Electronic Excitation and Density Response in Liquid Alkali Metals Studied by Inelastic X-ray Scattering

Dissertation

Department of Physics, Graduate School of Science
Kyoto University

Toru Hagiya

Abstract

Liquid metals can be regarded as a strongly interacting plasma consisting of electrons and ions, and the phenomenon of screening is important for understanding the effective interaction between the charged particles. The effective interaction is described by the dielectric function $\varepsilon(q, \omega)$, however, little information is available on $\varepsilon(q, \omega)$ of liquid metals. In this study, we have performed inelastic X-ray scattering (IXS) experiments on liquid alkali metals to investigate electronic excitations and static screening property.

First, we carried out the IXS experiments on liquid Rb at high temperatures to determine the excitation energy and line width of plasmon. Plasmon is a collective excitation of electrons, and the excitation energy $\hbar\omega_{\mathrm{p}}(q)$ is determined by the condition $\varepsilon(q, \omega_{\mathrm{p}}(q)) = 0$. We found that the density dependence of the plasmon energy in liquid Rb is well described by the electron gas model, however, the absolute value takes a lower value than the electron gas prediction. This disagreement is resolved by the calculation of the plasmon energy including the interband transition, which is described by liquid structure factor.

Then, we measured the IXS spectra of solid and liquid Li to determine the static density response function, which can describe screening electron density. We have experimentally demonstrated that the static density response function of the solid and liquid exhibits a $2k_F$ singularity, which reflects the sharp cutoff in the momentum distribution (k_F is the Fermi wave vector).

Valence electrons in alkali metals are regarded as a natural realization of the electron gas, and the experimental results enable valuable comparison with the electron gas model. Moreover, this study provides significant insight into the screening in liquid metals.

Contents

1 Introduction **4**

1.1 Fluid Alkali Metals 4

1.2 Inelastic X-ray Scattering 8

1.3 Purpose of This Study 11

2 Experimental **13**

2.1 Measurements for Rb 13

2.1.1 Sample Cell 13

2.1.2 Chamber for Scattering Experiment 14

2.1.3 Inelastic X-ray Scattering at SPring-8 15

2.1.4 Experimental Condition 16

2.2 Measurements for Li 17

2.2.1 Sample Cell 17

2.2.2 Inelastic X-ray Scattering at SPring-8 18

2.2.3 Experimental Condition 19

3 Plasmons in Liquid Rb at Elevated Temperatures **20**

3.1 Introduction to This Chapter 20

3.2 Plasmons and Particle-hole Pair Excitations in the Electron Gas Model 24

3.3 Derivation of the Plasmon Energy and Line Width in Liquid Metals . 26

3.3.1 Plasmon Energy at $q = 0$ with the Effect of Ionic Structure . . 26
3.3.2 Plasmon Line Width at Finite q with the Effect of Ionic Structure 28
3.4 Results 31
3.4.1 Data Analysis 31
3.4.2 IXS Spectra 32
3.5 Discussion 34
3.5.1 Plasmon Energy 34
3.5.2 Plasmon Line Width 40
3.6 Summary 44

4 Static Density Response Function of Li: $2k_F$ Singularity 45
4.1 Introduction to This Chapter 45
4.2 Results 49
4.2.1 Raw IXS Spectrum 49
4.2.2 Data Analysis 52
4.3 Discussion 56
4.3.1 Dynamic Structure Factor 56
4.3.2 Imaginary Part of the Density Response Function 59
4.3.3 Static Density Response Function 61
4.3.4 Screening Electron Density 65
4.3.5 Static Dielectric Function 68
4.4 Summary 69

5 Conclusion 70

Appendix A

A.1 Density Response Function

Appendix B

B.1 Lindhard Dielectric Function

B.2 Mermin Dielectric Function

B.3 Static Dielectric Function with Fermi Surface Blurring

Chapter 1

Introduction

1.1 Fluid Alkali Metals

Valence electrons in alkali metals are of fundamental interest as a natural realization of the electron gas. Extensive experimental efforts for alkali metals have been made for extracting information on many-body effects in the electron gas. The electron gas model provides a basic ingredient of the density-functional theory (DFT); the exchange-correlation (XC) energy of electron gas, which depends only on the electron density, is used for usual DFT calculations. Liquid-state alkali metals offer a valuable opportunity for investigating the behavior of the electrons in real metals as a function of the density. Figure 1.1 illustrates the pressure-temperature phase diagram of a typical alkali metal. If the liquid is pressurized and heated along the liquid-vapor coexistence line, a continuous density reduction becomes possible. Density of the fluid eventually becomes very close to that of the vapor phase near the critical point, and the supercritical state is realized.

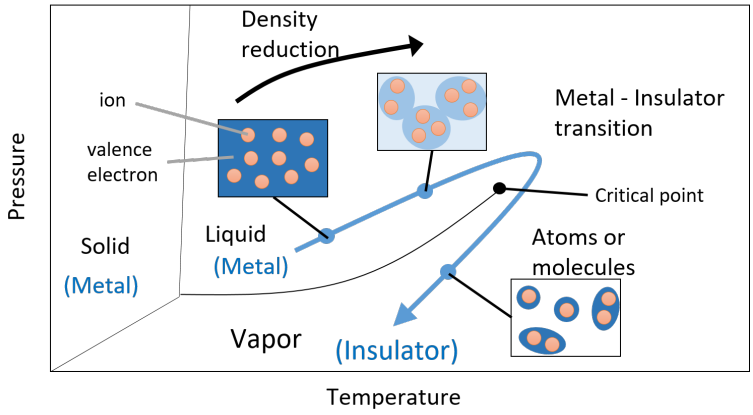

Figure 1.1: Temperature–pressure phase diagram of a typical alkali metal.

The electronic state of fluid alkali metals shows a drastic change depending on its density. Near the melting point, fluid alkali metals remain a good conductor; their electric resistivities are about 10^{-8} Ω m [1]. The electronic transport properties are well described with nearly free-electron (NFE) model [2]. However, as the fluid is expanded along the coexistence curve, the metallic character is gradually lost. Finally, a metal to non-metal transition occurs near the liquid-gas critical point. The microscopic mechanism has not been clarified yet. What should be noted is that the NFE picture starts to break down from an early stage of the volume expansion. Below about 3 times the critical density ρ_c, the resistivity [3] deviates from the NFE prediction. Moreover, approximately below $3\rho_c$, the magnetic susceptibility shows a distinct rise [4], and the effective mass determined by optical measurements becomes large compared with the free electron value [5]. These experimental change indicates the importance of electron-electron increases in the low-density region.

In the low-density fluid alkali metals, a spatial inhomogeneity of the electron and ion was observed. Figure 1.2 shows the average nearest-neighbor distance R_1 determined by X-ray diffraction measurements of Rb [6]. With decreasing density, R_1 starts to decrease between 3 - 4 ρ_c, in spite of volume expansion. Moreover, the

density fluctuation estimated from the small angle scattering intensity also grows from the same density region. These structural features mean that the spatial arrangement of liquid Rb becomes inhomogeneous with volume expansion. The electronic density distribution was also investigated by an *ab initio* molecular dynamics simulation [7], and the electron density at $3.3\rho_c$ exhibits spatially inhomogeneous distribution related to fluctuated atomic arrangement. The signature of the charge inhomogeneity was manifested in other observables; the electronic kinetic energy derived from the Compton profile [8] and the inelastic neutron scattering spectra of collective modes in liquid Rb [9].

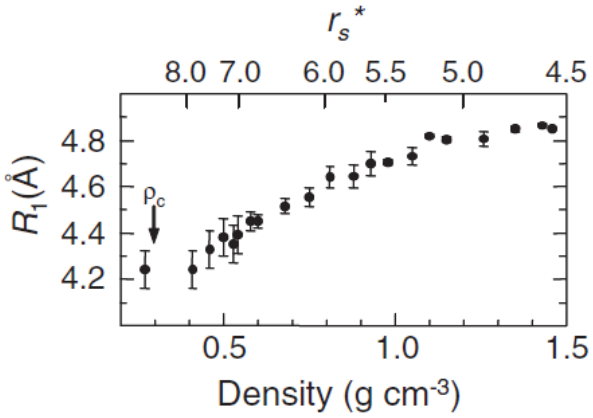

Figure 1.2: Density dependence of the average nearest-neighbor distance R_1. The critical density $\rho_c = 0.29$ gcm^{-3} is indicated by the arrow. (reprinted from Ref. [6])

Recently, it has been pointed that the charge inhomogeneity in expanded fluid alkali metal is closely connected to the instability of low-density electron gas [6,8,9]. The compressibility of the electron gas has been deduced from the accurate ground-state energy calculated by quantum Monte Carlo methods [10]. Figure 1.3(a) shows the r_s dependence of the inverse of the compressibility $1/\kappa$. r_s is the electron density parameter defined as:

$$r_{\rm s} = \left(\frac{3}{4\pi n}\right)^{1/3} / a_{\rm B}^{*}, \tag{1.1}$$

where n is the electron number density and $a_{\rm B}^{*} = \hbar^2 \varepsilon_{\rm b} / m_{\rm eff} e^2$ is the effective Bohr radius ($\varepsilon_{\rm b}$: static dielectric constant of the polarizable background, $m_{\rm eff}$: effective mass). The inverse of the compressibility $1/\kappa$ turns to be negative at $r_{\rm s} = 5.25$ [11]. The negative compressibility has a significant effect on the static dielectric function $\varepsilon(q, \omega = 0)$ via the compressibility sum rule [11]:

$$\lim_{q \to 0} \varepsilon(q, 0) = 1 + \frac{4\pi e^2 n^2}{q^2} \kappa. \tag{1.2}$$

Based on Eq. (1.2), the negative compressibility could lead to $\varepsilon(q, 0) < 0$ at a little q. Figure 1.3(b) shows the various theoretical calculations of $1/\varepsilon(q, 0)$ in the electron gas model. The RPA results are always positive, however, the results which include the XC effect become negative at high $r_{\rm s}$. The inequality $\varepsilon(q, 0) < 0$ drastically affects the effective interaction in the low-density electron gas; the interaction between like charges, $4\pi e^2 / [q^2 \varepsilon(q, 0)]$, becomes attractive [12]. Actually, the average nearest-neighbor distance of fluid Rb begins to decrease at about $r_{\rm s} = 5.25$ (See Fig. 1.2). This structural characteristics indicates that an attractive interionic force is enhanced because of $\varepsilon(q, 0) < 0$. However, the experimental information on the electronic state of fluid Rb is sparse, and the relation between the observed charge inhomogeneity and the instability of the electron gas is still not sufficiently clarified.

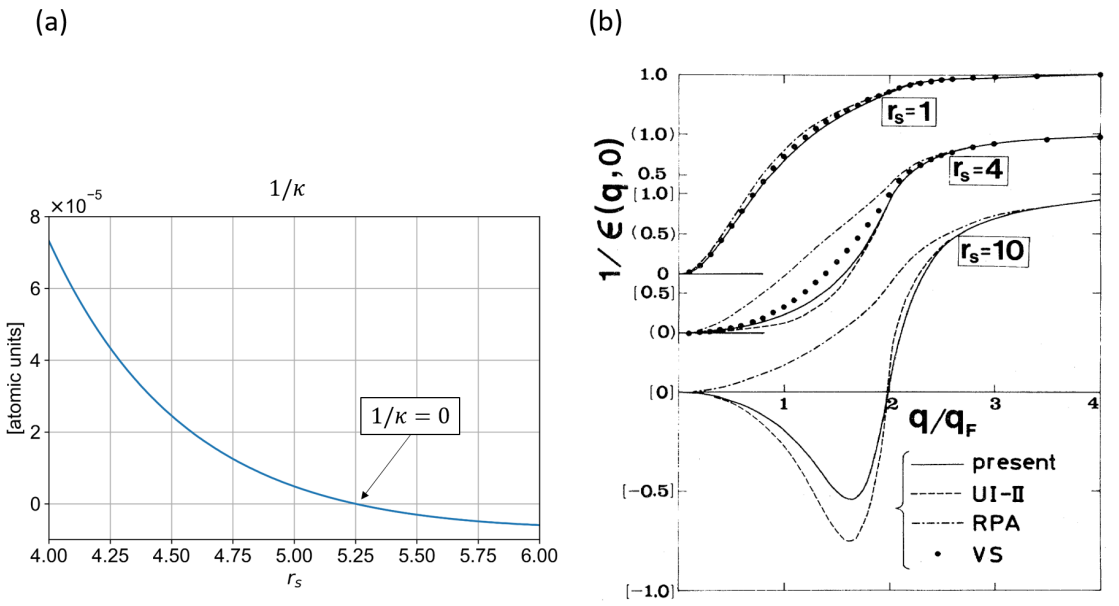

Figure 1.3: (a) Inverse of the compressibility in the electron gas model [11]. (b) The static dielectric function in the electron gas model at various r_s. The dashed and dotted curves represent the PRA results, and the other curves denote the results with XC effects (present: Ref. [13], UI-II: Ref. [14], and VS: Ref. [15]). (reprinted from Ref. [13])

1.2 Inelastic X-ray Scattering

We utilized inelastic X-ray scattering (IXS) technique to investigate the electronic state of liquid alkali metals. In IXS experiments, the incident X-ray with momentum $\hbar\boldsymbol{q}_1$ and energy $\hbar\omega_1$ is scattered by the sample. During the scattering process, the momentum $\hbar\boldsymbol{q} = \hbar\boldsymbol{q}_1 - \hbar\boldsymbol{q}_2$ and the energy $\hbar\omega = \hbar\omega_1 - \hbar\omega_2$ are transferred to the sample, where $\hbar\boldsymbol{q}_2$ and $\hbar\omega_2$ are the momentum and the energy of the scattered X-ray, respectively. In the experiments, the double-differential cross section, which depends on ω as well as $\boldsymbol{q}$, is measured. The double-differential cross section is expressed as [16]

$$\frac{d^2\sigma}{d\Omega d\omega} = \left(\frac{d\sigma}{d\Omega}\right)_{\mathrm{Th}} S(\boldsymbol{q},\omega), \tag{1.3}$$

where $(d\sigma/d\Omega)_{\mathrm{Th}}$ and $S(\boldsymbol{q},\omega)$ are the Thomson cross section and dynamic structure factor, respectively. The dynamic structure factor, which is the Fourier transform in space and time of the time-dependent density-density correlation function, contains information on the electronic excitation in materials. Depending on the scale of $\hbar\omega$, various excitations are observed, such as phonons, plasmons, electron-hole pair excitations, and core-electron excitations. In this study, we focus on the energy range of 10^0 – 10^2 eV, where the spectrum is dominated by electronic excitations.

IXS is a powerful tool for studying the electronic excitations of a matter over a wide range of thermodynamic state. The electronic excitations can be also obtained by electron energy-loss spectroscopy (EELS), however, EELS requires vacuum environment and is not suited for the measurement of liquid samples. IXS can be applied to a matter under extreme conditions at high temperatures [17,18] and high pressures [19,20].

Recently, the development of IXS techniques has allowed the determination of the density response function of electrons [21,22]. The density response function $\chi(\boldsymbol{q},\omega)$ describes the electron density induced by external potential $V_{\mathrm{ext}}(\boldsymbol{q},\omega)$ as $\Delta n(\boldsymbol{q},\omega) = \chi(\boldsymbol{q},\omega)V_{\mathrm{ext}}(\boldsymbol{q},\omega)$, where $\Delta n(\boldsymbol{q},\omega)$ is the induced electron density. The theoretical foundation of the density response function is described in the Appendix A.1. The dynamic structure factor is related to the imaginary part of the density response function via the fluctuation dissipation theorem [16]:

$$\mathrm{Im}[\chi(\boldsymbol{q},\omega)] = -\pi\left(1-\exp\left[-\hbar\omega/(k_{\mathrm{B}}T)\right]\right)S(\boldsymbol{q},\omega) \approx -\pi S(\boldsymbol{q},\omega), \tag{1.4}$$

where k_{B} is the Boltzmann constant. In the energy scale of this study (10^0 – 10^2 eV), it is considered to be $\exp\left[-\hbar\omega/(k_{\mathrm{B}}T)\right] \approx 0$. In addition to the density response function, dielectric function is an important quantity for describing dielectric screening, and it describes how bare potential is screened to give effective potential as $V_{\mathrm{eff}}(\boldsymbol{q},\omega) = V_{\mathrm{ext}}(\boldsymbol{q},\omega)/\varepsilon(\boldsymbol{q},\omega)$. The density response function is related

to the dielectric function via the following equation [23]:

$$\frac{1}{\varepsilon(\boldsymbol{q},\omega)} = \frac{4\pi e^2}{q^2}\chi(\boldsymbol{q},\omega) + 1, \tag{1.5}$$

which is derived using Poisson's equation. Thus, $S(\boldsymbol{q},\omega)$ can be expressed in terms of $\varepsilon(\boldsymbol{q},\omega)$:

$$S(\boldsymbol{q},\omega) \approx -\frac{q^2}{4\pi^2 e^2}\mathrm{Im}\left[\frac{1}{\varepsilon(\boldsymbol{q},\omega)}\right]. \tag{1.6}$$

Only the imaginary is available from IXS measurements, however, the real part can be reconstructed by the Kramers–Kronig (K–K) transformation: [21]

$$\mathrm{Re}[\chi(\boldsymbol{q},\omega)] = \frac{1}{\pi}P\int_{-\infty}^{\infty} d\omega' \frac{\mathrm{Im}[\chi(\boldsymbol{q},\omega')]}{\omega' - \omega}. \tag{1.7}$$

Utilizing this procedure, Abbamonte *et al.* determined the density response function of water [21] and LiF [24]. They calculated $\chi(\boldsymbol{r},t)$ with the Fourier transform of $\chi(\boldsymbol{q},\omega)$ to discuss the attosecond electron dynamics in condensed matter [21,22,24]. In addition to the dynamical property, the *static* density response function $\chi(\boldsymbol{q},\omega = 0)$ can be extracted from the experimentally obtained *dynamic* structure factor. Reed *et al.* determined $\chi(\boldsymbol{q},\omega = 0)$ by setting $\omega = 0$ in Eq. (1.7) and investigated the *static* screening property of graphene [25].

In order to determine the density response function, the accurate measurement of IXS spectra over wide $\boldsymbol{q}$ and ω range is essential, which has been made possible by recent progress in IXS techniques in the following points. (i) Since the third-generation synchrotron radiation sources became available in the 1990s, the spectrometers and detectors for IXS experiments have developed significantly. (ii) The stable intensity of synchrotron radiation source was realized because of the top-up operation at synchrotron radiation facilities.

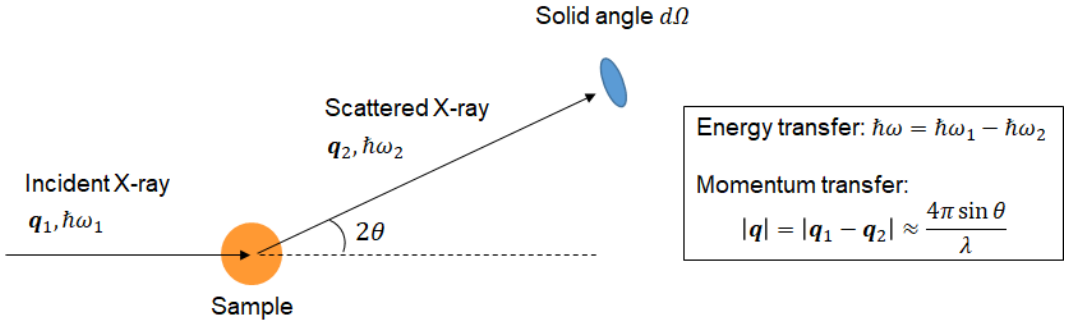

Figure 1.4: Schematic drawing of the inelastic X-ray scattering (See text).

1.3 Purpose of This Study

Our ultimate purpose is to reveal the relation between the electronic state of expanded fluid alkali metals and the instability of the electron gas. Previous studies suggested that the charge inhomogeneity occurring in the expanded fluid alkali metals is caused by the negative $\varepsilon(q, 0)$, which was predicted in the low-density electron gas. However, it is difficult to obtain experimental information on the dielectric function for the fluid, and the origin of the charge inhomogeneity has not been elucidated.

IXS is a powerful tool for investigating information on dielectric screening, because the IXS spectra is proportional to $\mathrm{Im}[1/\varepsilon(\boldsymbol{q}, \omega)]$ and $\mathrm{Im}[\chi(\boldsymbol{q}, \omega)]$ (See Eq. (1.4) and (1.6)). The purpose of this thesis is to lay the foundation of an experimental approach for investigating the electronic excitation and static screening of liquid metals. Thus, we have performed two IXS experiments on liquid alkali metals. First, we measured IXS spectra of liquid Rb at 573 and 773 K to investigate the plasmon, focusing on the electronic excitation. We investigated how the structural change in the liquid influences the plasmon energy and line width. Then we measured IXS spectra of solid and liquid Li over wide range of q and ω, and determined

the static density response function of a simple metal for the first time. We deduced information on the static screening from the response function.

In the next Chapter (Chapter 2), the detail of the experimental method is explained. In Chapter 3, the results of IXS measurements for liquid Rb are presented. The density dependence of the plasmon energy and line width are discussed with the aid of theoretical calculation. In Chapter 4, the results of IXS measurements for solid and liquid Li are presented. From the IXS spectra, we determined the static density response function and discussed the static screening property. Finally, conclusions are drawn in Chapter 5. In the thesis, we measured liquid or polycrystalline samples, which is considered to be isotropic. Hereafter, we will represent the physical quantities such as, the dynamic structure factor and density response function, with $q = |\boldsymbol{q}|$. We will use cgs units throughout the thesis.

Chapter 2

Experimental

2.1 Measurements for Rb

2.1.1 Sample Cell

In order to carry out IXS experiments for liquid Rb, we made a single crystal sapphire cell [26]. Single crystal sapphire is resistant to the chemical corrosion of liquid alkali metals. Figure 2.1 shows the cross sectional diagram for the sapphire cell. The cell components were connected with a ceramic adhesive. There are holes in the ring and outer pipe so that liquid sample can be introduced from the sample reservoir to the sample space. The cell windows were polished to 150 μm to reduce the background signal of the cell. In order to optimize scattering intensity, the sample thickness was set to be 300 μm, which is close to the X-ray attenuation length of Rb at 13.8 keV.

We used high-purity (99.9 %) Rb and handled the sample in a helium filled glovebox to avoid the oxidation of the sample. The liquid sample was introduced into the sample space by pressurizing the liquid surface formed in the sample reservoir. The complete seal of the cell is important for the introduction, and we checked that there is no leakage with a helium leak detector. The detail procedure of the leak test and the sample introduction are described in Ref. [27].

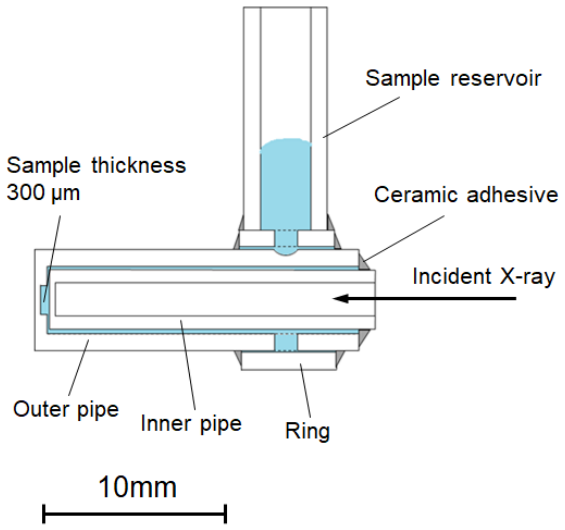

Figure 2.1: Cross sectional diagram for the sapphire cell.

2.1.2 Chamber for Scattering Experiment

Figure 2.2 shows the cross sectional diagram of the chamber for scattering experiment. During scattering experiments, the sample cell was set in the chamber, which was filled with helium gas. We used aluminum foils for the X-ray windows, and the thickness of the foils is 100 μm. The chamber can be pressurized up to 0.5 MPa, which is useful for the improvement of the sample filling in the sample space.

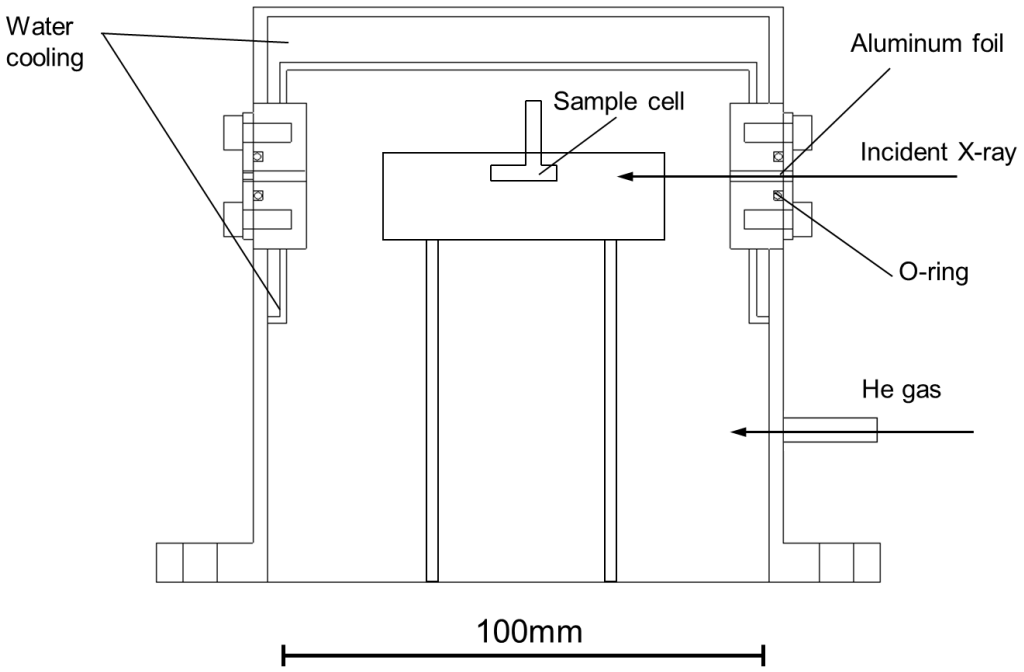

Figure 2.2: Cross sectional diagram for the chamber.

2.1.3 Inelastic X-ray Scattering at SPring-8

We carried out IXS measurements at the Taiwan IXS beam line BL12XU at SPring-8 [28]. Figure 2.3 shows the layout of IXS experiments. The incident photon beam was monochromated with a combination of a Si(111) double crystal monochromator and a Si(400) four-bounce high resolution monochromator. The energy of incident X-ray was 13.8 keV. The measurements were performed using a spherical crystal analyzer and a Si detector in a near backscattering geometry. The energy resolution was 0.22 eV, which was determined from the full width at half maximum (FWHM) of the elastic peak.

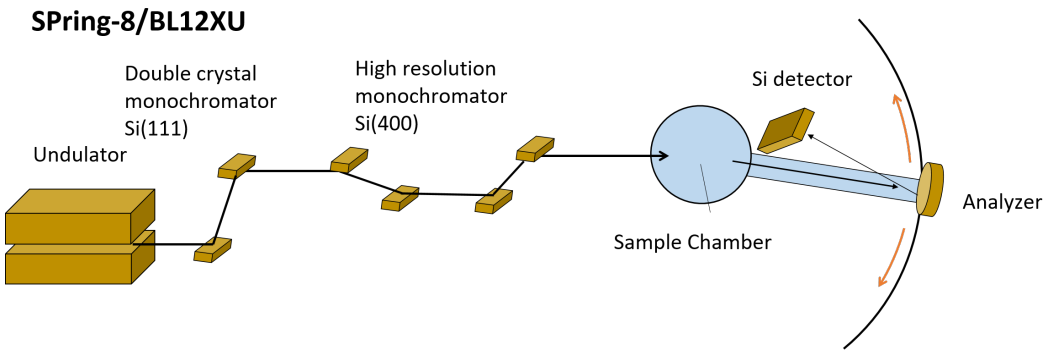

Figure 2.3: Layout of the Taiwan inelastic x-ray scattering beamline BL12XU at SPring-8 for measurement of Rb.

2.1.4 Experimental Condition

The IXS measurements were performed at two temperatures, 573 and 773 K. We used a chamber with windows of Kapton film [27] for the measurement at 573 K. For the measurement at 773 K, we used the chamber with windows of aluminum foils and pressurized the sample at 0.26 MPa for keeping the high-temperature liquid stable in the sample space. The cell was heated by the Fe-Cr heater (diameter 0.40 mm) and the temperature was monitored with alumel-chromel thermocouples.

The scanned range of the energy transfer was from 0.5 eV to 6.5 eV. The IXS spectra were collected in the range 0.28 - 0.80 Å^{-1}. After measuring the IXS signal of the sample, we also measured the IXS signal of an empty cell set in the chamber to estimate the background. In the case of the chamber with Kapton windows, the background was negligible. However, a small background was detected in the case of the chamber with aluminum windows. We subtracted the background in the latter case.

2.2 Measurements for Li

2.2.1 Sample Cell

Figure 2.4(a) shows the metallic cell for IXS measurements of Li. The sample was contained in the reservoir made of molybdenum (Mo), which has a resistance to the chemical corrosion of liquid alkali metals. The stainless steel flange has an edge, and the liquid sample was sealed with the Mo foils and the edge. The thickness of the Mo foil was 10 μm, and the sample thickness was 3 mm.

The metallic cell was heated by Fe-Cr heater with diameter of 0.40 mm. Figure 2.4(b) shows a construction of the heating system. The Fe-Cr wire was cover by alumina tubes with inner diameter of 0.5 mm and outer diameter of 1.0 mm. The side of the metallic cell was surrounded by the heater. The temperature of the cell was monitored with alumel-chromel thermocouples which were inserted into the holes in the metallic cell.

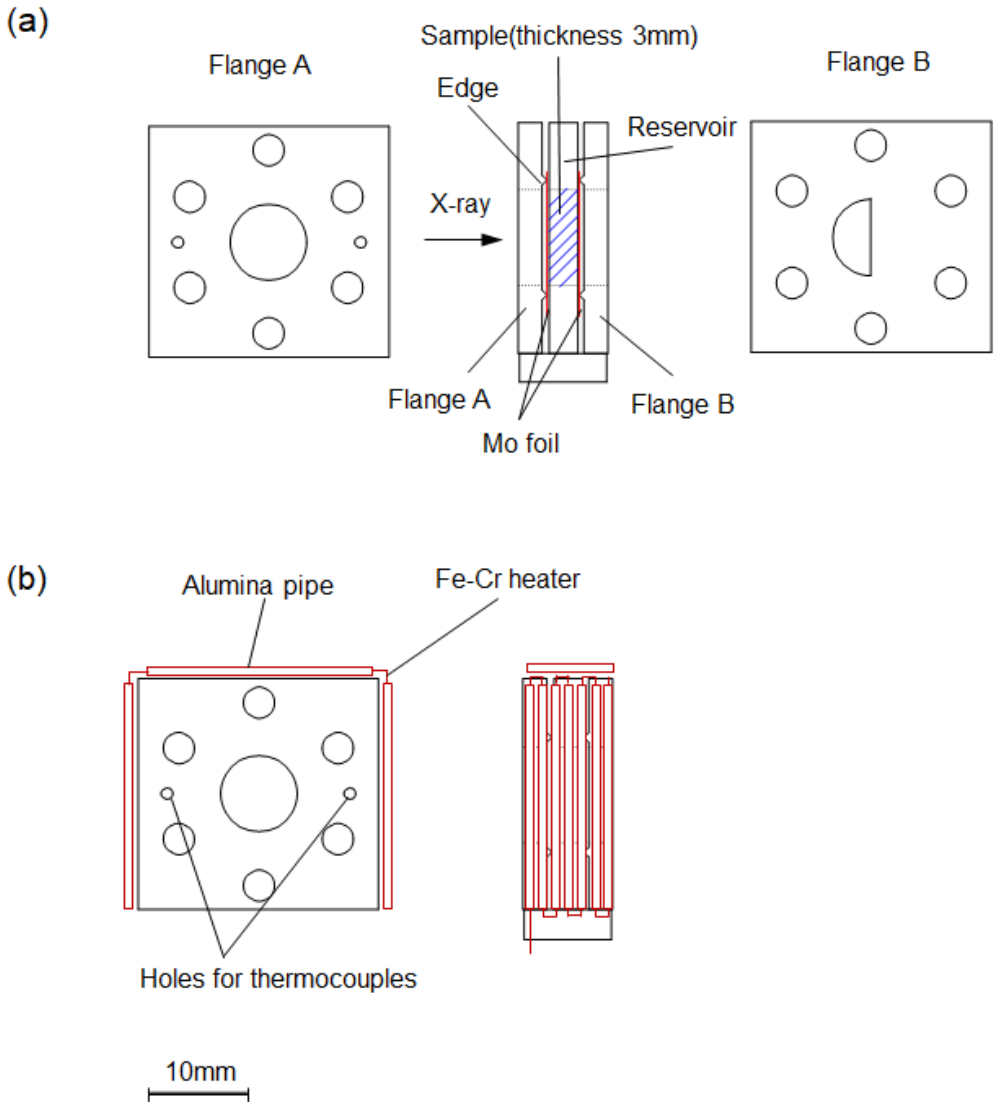

Figure 2.4: (a) Metallic cell for the IXS measurement of Li. (b) Schematic diagram of the heating system.

2.2.2 Inelastic X-ray Scattering at SPring-8

We performed IXS experiments at the beamline BL12XU. Figure 2.5 shows the layout of IXS beamline BL12XU for the measurements of Li. The synchrotron

radiation from an undulator source was monochromated by a cryogenic Si (111) double crystal and a pair of Si (220) channel-cut crystals. The energy of incident X-ray was fixed at 19.98 keV. The scattered X-ray was reflected by a Si (660) triangular crystal and counted by an NaI scintillation detector [29]. The energy resolution varied in 1.2 - 1.4 eV, depending on the scattering angle. Although the energy resolution is lower than that in the measurement of Rb, we can obtain a stronger signal of IXS. This setup is suitable for performing the K–K analysis, because it is necessary to measure IXS spectra over a wide energy range.

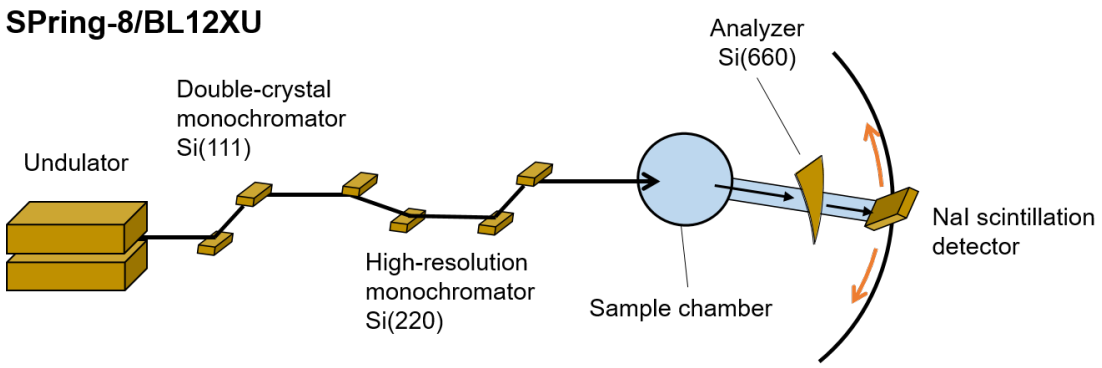

Figure 2.5: Layout of the Taiwan inelastic x-ray scattering beamline BL12XU at SPring-8 for measurement of Li.

2.2.3 Experimental Condition

The IXS measurements were performed for polycrystalline Li (RT) and liquid Li (493 K). The sample cell was contained in the chamber with aluminum windows. We collected 19 spectra in the range of 0.30 - 3.47 Å^{-1}. In $0.30 < q < 0.80$ Å^{-1}, IXS spectra were scanned in the energy transfer range of -10 eV to 110 eV. In $1.01 < q < 3.47$ Å^{-1}, the energy scan was performed in the energy transfer range of -10 eV to 350 eV. The measured range of the IXS spectra very wide compared to usual IXS experiments [30–35] for the purpose of the K–K transformation.

Chapter 3

Plasmons in Liquid Rb at Elevated Temperatures

3.1 Introduction to This Chapter

Plasma oscillation is a fundamental electronic excitation and can be observed in a wide range of materials such as ionized gas, warm dense matter, metals, and semiconductors. Especially in metals, electron-electron interaction plays an essential role for describing the plasma oscillation, and a quantum of the oscillation is called a plasmon. A basic understanding of the plasmon was provided by the electron gas model within the random phase approximation (RPA) [36]. Even today, the construction of a sophisticated theory for many-body effects on plasmons remains a challenge in condensed matter physics [11].

Various theories for the plasmons can be tested by EELS or IXS measurements. EELS measurements by vom Felde and co-workers [37] revealed that the plasmon energies of alkali metals deviate from that of the electron gas model, even with the XC effects included. Figure 3.1 shows the plasmon energy dispersion of solid Rb and Cs. The experimentally obtained plasmon energy takes values lower than those

predicted in the electron gas model. In addition to the absolute value, the qualitative q dependence does not agree with the calculated results; the dispersion curve of Rb bents around $q^2 = 0.4$ Å^{-2} and Cs shows a negative dispersion. Aryasetiawan and Karlsson carried out *ab initio* calculation for solid alkali metals and determined the plasmon dispersion [38]. They showed that an effect of interband transition (the band structure effect) lowers the plasmon energy and causes a negative dispersion in the case of Cs. The band structure effect arises from the periodic lattice potential and is essential for describing plasmon behaviors in various crystalline metals such as Be [39], K [40], Al [41], and Pb [42].

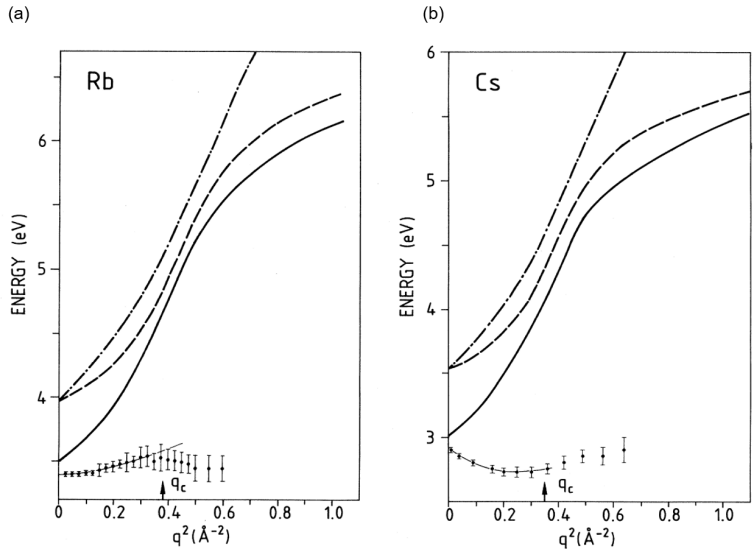

Figure 3.1: (a) Plasmon energy dispersion of solid Rb. (b) Plasmon energy dispersion of solid Cs. Dash-dotted line: The plasmon energy of the electron gas within the RPA. Dashed line: the same with inclusion of a XC effect using a local field correction by Vashishta and Singwi [15]. Solid line: the same with inclusion of a core polarizability. (reprinted from Ref. [37])

IXS measurements revealed that the band structure effect is also present in the liquid state. Figure 3.2(a) shows the plasmon dispersion of solid and liquid Li measured by Hill *et al.* [35]. The plasmon energy of liquid Li is slightly smaller than that of the solid, which can be simply explained by the density change upon melting.

The downward energy shift relative to the electron gas prediction, which is caused by the band structure effect, remains in the liquid state. Thus, they pointed out that the band structure effect resulting from ionic structure still exists in the liquid state. In this study, we express the band structure effect in the liquid state as the effect of ionic structure. This effect is also important for describing the experimentally obtained plasmon energy in other liquid metals such as Al [43], Rb [44], and Cs [45]. However, the shape of the plasmon dispersion changes on melting in heavy alkali metals (Rb and Cs), unlike the case of Li, and the effect of ionic structure on the plasmon energy has not fully understood.

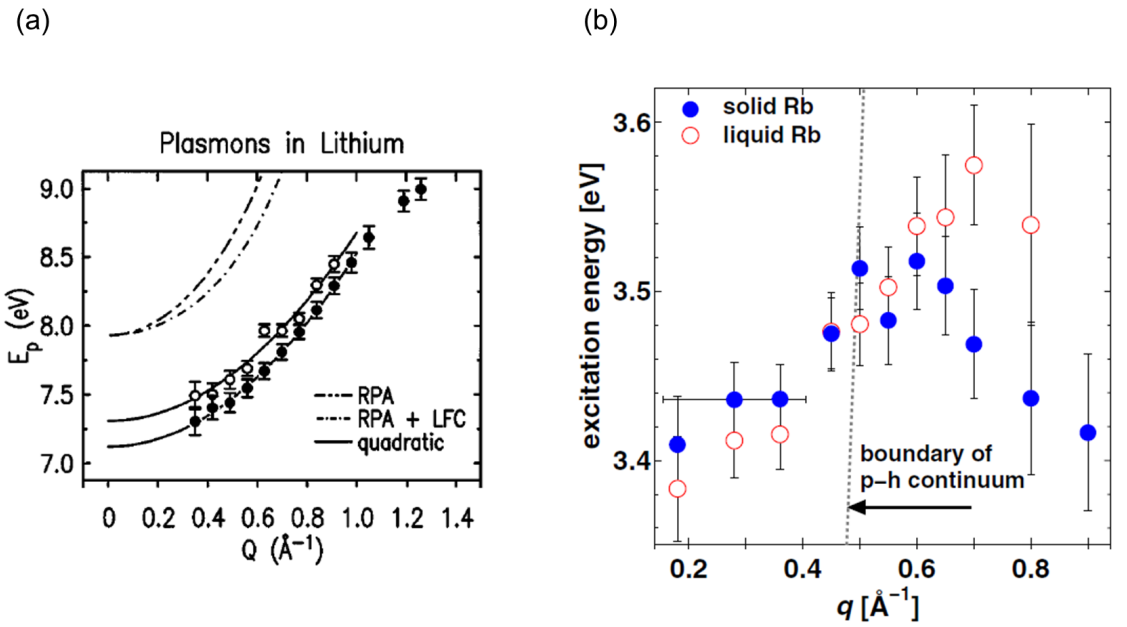

Figure 3.2: (a) Plasmon energy of solid and liquid Li. The open and closed circles represent the plasmon energy of the solid and liquid, respectively. The calculated results of the electron gas with the RPA and XC effects are also plotted. (reprinted from Ref. [35]) (b) Plasmon energy of solid and liquid Rb. The dotted line indicates the boundary of particle-hole continuum. (reprinted from Ref. [44])

In liquid metals the effect of ionic structure is a main cause of the plasmon damping. Kimura *et al.* theoretically investigated the plasmon damping by ionic

potential, and derived a formula to calculate the plasmon line width of simple liquid metals [46]. In this formula, the effect of ionic structure is expressed by a pseudopotential and liquid structure factor $S(q)$. The derived formula well reproduces experimental results of liquid alkali metals [44, 46].

The plasmon of liquid metals has thus far been observed only near the melting point, and how the variation in the ionic structure influences the plasmon behaviors has not been clarified sufficiently. For a profound understanding of the effect of ionic structure, it is significant to perform IXS experiments at high temperatures beyond the melting point. Structural information of liquids is reflected in $S(q)$, and the shape of $S(q)$ systematically changes with temperature. Thus, the observation of plasmons at high temperatures enables us to reveal the relation between the plasmon behaviors and ionic structure.

In this study, we carried out IXS measurements on liquid Rb at 573 and 773 K to determine the plasmon energy and line width. This chapter is organized as follows. In Sec. 3.2., the plasmon energy and line width of the electron gas model are explained. In Sec. 3.3, we derive a formula to calculate the plasmon energy at $q = 0$ and plasmon line width at $q \neq 0$ of liquid metals. In previous work by Kimura *et al.* [46], only the plasmon line width at $q = 0$ was formulated. In Sec. 3.4, we show the raw IXS spectra and the procedure to determine the plasmon energy and line width. In Sec. 3.5, we discuss the temperature (and density) dependence of the plasmon behavior of liquid Rb. Finally in Sec. 3.6, we present the summary of this chapter.

3.2 Plasmons and Particle-hole Pair Excitations in the Electron Gas Model

The plasmon energy $\hbar\omega_{\rm p}(q)$ is determined by the condition $\varepsilon(q,\omega_{\rm p}(q))=0$, which means that a density fluctuation arises without external potential. Electronic excitations like a plasmon or a particle-hole (p-h) pair excitations can be observed in an IXS spectrum, because $S(q,\omega)$ is related to $\varepsilon(q,\omega)$ via the following equation:

$$S(q,\omega) = -\frac{q^2}{4\pi^2 e^2}\mathrm{Im}\left[\frac{1}{\varepsilon(q,\omega)}\right]. \tag{3.1}$$

Figure 3.3 shows the $S(q,\omega)$ of the electron gas model within the RPA, which is calculated by the Lindhard dielectric function $\varepsilon_{\rm L}(q,\omega)$ [47]. The analytic expression for $\varepsilon_{\rm L}(q,\omega)$ is given in the Appendix B.1. In low q region, $S(q,\omega)$ has poles at $\omega=\omega_{\rm p}(q)$ and is expressed as [11]:

$$S(q,\omega) \approx \frac{\omega_{\rm p}(q)}{8\pi} q^2 \delta(\omega-\omega_{\rm p}(q)) \qquad (q<q_c), \tag{3.2}$$

where the definition of cutoff wave vector q_c is given in the caption of Fig. 3.3. In the RPA, the plasmon line width is zero and the plasmon is not damped. The plasmon energy dispersion is written as:

$$\hbar\omega_{\rm p}^{\rm RPA}(q) = \hbar\omega_{\rm p} + \frac{\hbar^2}{m_{\rm eff}}\alpha_{\rm RPA} + O(q^4), \tag{3.3}$$

where $\alpha_{\rm RPA}$ is the dispersion coefficient and $\hbar\omega_{\rm p}=\hbar\sqrt{4\pi n e^2/\varepsilon_{\rm b} m_{\rm eff}}$ is the plasmon energy in the long-wavelength limit (n : electron density, e: electron charge, $m_{\rm eff}$: effective mass, $\varepsilon_{\rm b}$: static dielectric constant). Dynamic XC effects beyond the RPA should be taken into account in the plasmon, and the plasmon energy is modified

by the dynamic local field correction $G(q,\omega)$ [11]:

$$[\hbar\omega_{\rm p}^{\rm eg}(q)]^2 = [\hbar\omega_{\rm p}]^2 + \frac{\hbar^2}{m_{\rm eff}}\left[\frac{6}{5}E_{\rm F} - \frac{4\pi e^2 n}{q^2}G(q,\omega)\right]q^2 + O(q^4), \tag{3.4}$$

where $E_{\rm F}$ is the Fermi energy. In high q region, the plasmon is no more well defined and decays into a particle-hole pair excitation. This mechanism of the damping is called Landau damping. In p-h pair excitation continuum, $S(q,\omega)$ is dominated by a p-h pair excitation with a wide line width.

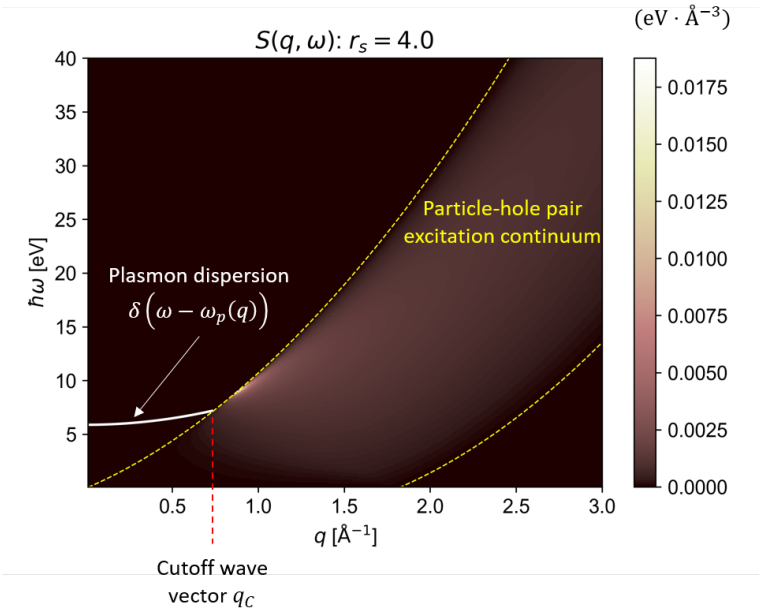

Figure 3.3: Dynamic structure factor $S^{\rm RPA}(q,\omega)$ of the electron gas within the RPA, which is calculated with $r_{\rm s} = 4.0$. The dashed lines are the boundary of p-h continuum. The plasmon dispersion curve intersects with the boundary at cutoff wave vector q_c.

Calculation Condition

For comparison with the experimental results of liquid Rb, We calculated the plasmon energy of the electron gas model based on Eq. (3.4). In the calculation of

$\hbar\omega_{\rm p}^{\rm eg}(q)$, dynamic local field correction $G(q,\omega)$ was approximated by static local field correction $G(q,0)$. We used the static local field correction of Ref. [48], which is obtained with quantum Monte Carlo simulation. The static local field correction is parameterized by $r_{\rm s}$, and its $r_{\rm s}$ dependence is presented in Ref. [49].

The electron density n was estimated from the fluid density of Rb. The static dielectric constant $\varepsilon_{\rm b}$ is given by $\varepsilon_{\rm b} = 1+4\pi n_{\rm i}\chi_{\rm i}$, where $n_{\rm i}$ is the ionic density and $\chi_{\rm i}$ is the ionic polarizability. We set $\chi_{\rm i} = 8.986$ (atomic units), the value calculated by Chattopadhyay *et al.* [50]. In the temperature range of this study, the effective mass of liquid Rb is almost equal to free electron mass m [5], and we assumed $m_{\rm eff} = m$.

3.3 Derivation of the Plasmon Energy and Line Width in Liquid Metals

3.3.1 Plasmon Energy at $q = 0$ with the Effect of Ionic Structure

In this section, we derive an equation to calculate the plasmon energy with the effect of ionic structure $\hbar\omega_{\rm p}^{\rm ion}(q=0)$, based on the method of Ref. [46]. The plasmon line width of liquid simple metals is expressed as [46]

$$\Delta E_{1/2}^{\rm ion}(0) = \hbar\omega_{\rm p}\frac{4}{3n_{\rm ion}(\hbar\omega_{\rm p}/E_{\rm F})^4}\int\frac{d^3q'}{(2\pi)^3}\left(\frac{q'}{k_{\rm F}}\right)^4 \times \left|v_{\rm ion}^{\rm s}(q)\right|^2 S(q')\mathrm{Im}[\varepsilon_{\rm L}(q',\omega_{\rm p})], \tag{3.5}$$

where $v_{\rm ion}^{\rm s}(q)$ is the screened ionic potential. The information of liquid ionic structure is included in $S(q)$. The mechanism of the plasmon damping in $q < q_{\rm c}$ is illustrated in Fig. 3.4. According to the electron gas model within the RPA, the plasmon dose not damp in $q < q_{\rm c}$. However, for the solid state, if the reciprocal lattice vector is located in the p-h continuum, the plasmon can decay into a p-h pair excitation by gaining the momentum from the lattice (the Umklapp process) [51]. For the liquid

state, well-defined reciprocal lattice does not exit, and the momentum transfer from q_1 to q_2 is involved in the plasmon damping thorough $S(q)$ [27] (See Fig. 3.4).

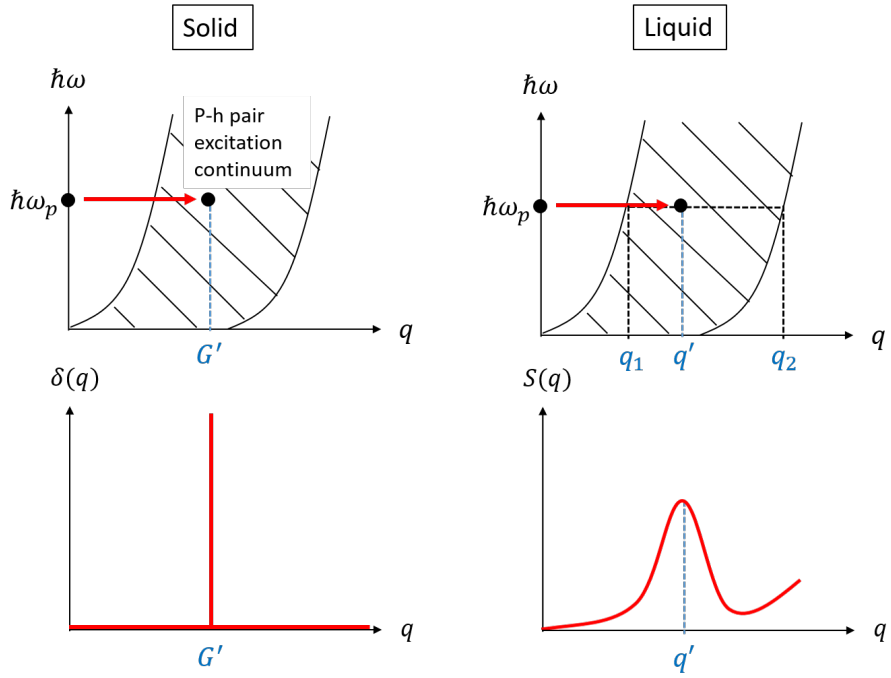

Figure 3.4: Schematic illustration of the mechanism of plasmon damping in solid and liquid state.

For the calculation of the plasmon energy, we derive the real part of the dielectric function. The dielectric function in the long-wavelength limit is written as [52]

$$\varepsilon(0,\omega) = 1 - \left(\frac{\omega_{\mathrm{p}}}{\omega}\right)^2 - \frac{4\pi}{\omega^2}\Pi(0,\omega), \tag{3.6}$$

where $\Pi(q,\omega)$ is the current-current correlation function. Based on the NFE, the current-current correlation function is expressed as [52]

$$\Pi(0,\omega) = \frac{1}{4\pi m^2\omega^2}\sum_{\boldsymbol{q}'}\frac{q'^4}{3}\left[\frac{1}{\varepsilon_{\mathrm{L}}(\boldsymbol{q}',\omega)} - \frac{1}{\varepsilon_{\mathrm{L}}(\boldsymbol{q}',0)}\right] \times \langle\Phi(\boldsymbol{q}')\Phi(-\boldsymbol{q}')\rangle, \tag{3.7}$$

where $\Phi(\boldsymbol{q}')$ describes the ionic potential in this case. We use the expression for $\Phi(\boldsymbol{q}')$ in Ref. [46], and the real part of the dielectric function in liquid metals is obtained from Equation (3.6):

$$\begin{aligned}\mathrm{Re}[\varepsilon^{\mathrm{ion}}(0,\omega)] =& 1 - \left(\frac{\omega_{\mathrm{p}}}{\omega}\right)^2 - \frac{4}{3n_{\mathrm{ion}}(\hbar\omega/E_{\mathrm{F}})^4}\int \frac{d^3q'}{(2\pi)^3} \\ & \times \left(\frac{q'}{k_{\mathrm{F}}}\right)^4 \left|\frac{v_{\mathrm{ion}}(q')}{E_{\mathrm{F}}}\right|^2 S(q') \\ & \times \mathrm{Re}\left[\frac{1}{\varepsilon_{\mathrm{L}}(q',\omega)} - \frac{1}{\varepsilon_{\mathrm{L}}(q',0)}\right]. \end{aligned} \tag{3.8}$$

In Eq. (3.8) the first and second terms corresponds to the contribution from the electron gas and the third represents the effect of ionic structure. The q integration is carried out inside the p-h continuum ($q_1 < q < q_2$). $\hbar\omega_{\mathrm{p}}^{\mathrm{ion}}(0)$ can be calculated with the condition $\mathrm{Re}[\varepsilon^{\mathrm{ion}}(0,\omega)] = 0$.

3.3.2 Plasmon Line Width at Finite q with the Effect of Ionic Structure

In this section, we derive a formula for the plasmon line width of liquid metals at finite q by modifying the formula in crystalline solids [53]. In the previous work [46], the formula at $q = 0$ was obtained. Based on the NFE approximation, the imaginary part of the dielectric function in crystalline solids for $|\boldsymbol{k}| < |\boldsymbol{k}_{\mathrm{c}}|$ ($\boldsymbol{k}_{\mathrm{c}}$ is the cutoff wave vector) is written as [53]

$$\begin{aligned}\mathrm{Im}[\varepsilon^{\mathrm{sol}}(\boldsymbol{k},\omega)] =& \frac{3\omega_{\mathrm{p}}^2}{8k^2}\sum_{\boldsymbol{G}} \frac{|v_{\mathrm{ion}}^{\mathrm{s}}(\boldsymbol{G})|^2}{2q} \\ & \times \left[L_1\left(\frac{\omega - q^2}{2q}\right)\theta\left\{1 - \left(\frac{\omega - q^2}{2q}\right)^2\right\}\right. \\ & \left. - L_2\left(-\frac{\omega + q^2}{2q}\right)\theta\left\{1 - \left(\frac{\omega + q^2}{2q}\right)^2\right\}\right], \end{aligned} \tag{3.9}$$

with

$$
\begin{aligned}
L_1(x) &= \frac{\pi}{2k_\perp^2}\left(\frac{\psi_1^2}{\sqrt{1-\psi_1^2}}+\frac{\psi_2^2}{\sqrt{1-\psi_2^2}}-\frac{(\psi_1+\psi_2)^2}{\sqrt{1-\psi_1^2}+\sqrt{1-\psi_2^2}}\right)\\
\psi_{1,2}(x) &= 2k_\perp\sqrt{1-x^2}/\alpha_{1,2}(x)\\
\alpha_1(x) &= \omega - k^2 - 2k_\parallel x\\
\alpha_2(x) &= \omega + k^2 - 2k_\parallel q - 2k_\parallel x\\
\theta(x) &= \begin{cases} 1 & (x>0)\\ 0 & (x<0). \end{cases}
\end{aligned}
\tag{3.10}
$$

$v_{\rm ion}^{\rm s}(\boldsymbol{G})$ is the screened crystal potential, and $k_\parallel$ and $k_\perp$ represent the vector component of $\boldsymbol{k}$ parallel and perpendicular to $\boldsymbol{q}=\boldsymbol{k}+\boldsymbol{G}$, respectively. $L_2(x)$ is the same expression as $L_1(x)$ except that the expression for $L_2(x)$ is given by replacing ω by $-\omega$ in the definitions of $\alpha_{1,2}$. The summation in Eq. (3.9) is taken over $\boldsymbol{G}$ satisfying the condition that $\boldsymbol{q}$ is located inside the p-h continuum. In the above equations, all energies and wave vectors are expressed in units of $E_{\rm F}$ and $k_{\rm F}$, respectively, and $\hbar$ and $2m$ are set to be 1 for simplicity.

The effect of the ionic potential in liquid metals can be expressed with the liquid structure factor, and the summation in Eq. (3.9) is replaced with the following integral:

$$
\sum_{\boldsymbol{G}} \left|v_{\rm ion}^{\rm s}(\boldsymbol{G})\right|^2 \to \frac{1}{n_{\rm ion}(2\pi)^3}\int d^3G\left|v_{\rm ion}^{\rm s}(G)\right|^2 S(G), \tag{3.11}
$$

where the effect of the ionic potential is weighted by the liquid structure factor. From Eq. (3.9) and (3.11), we obtain the imaginary part of the dielectric function

in liquid metals:

$$\begin{aligned}\mathrm{Im}[\varepsilon^{\mathrm{ion}}(k,\omega)] = \frac{3\omega_{\mathrm{p}}^2}{64\pi^2 n_{\mathrm{ion}} k^2} \int dG \int_0^{\pi} d\theta \frac{G^2 \left|v_{\mathrm{ion}}^{\mathrm{s}}(q)\right|^2 S(G) \sin\theta}{q} \\ \times \left[L_1\left(\frac{\omega - q^2}{2q}\right)\theta\left\{1 - \left(\frac{\omega - q^2}{2q}\right)^2\right\} \right. \\ \left. -L_2\left(-\frac{\omega + q^2}{2q}\right)\theta\left\{1 - \left(\frac{\omega + q^2}{2q}\right)^2\right\}\right], \end{aligned} \tag{3.12}$$

where θ is the angle between $\boldsymbol{k}$ and $\boldsymbol{G}$. The plasmon line width of liquid metals at finite q is calculated from the following relation [51]:

$$\Delta E_{1/2}^{\mathrm{ion}}(q) = 2\hbar \left[\left. \frac{\partial \mathrm{Re}[\varepsilon_{\mathrm{L}}(q,\omega)]}{\partial\omega} \right|_{\omega=\omega_{\mathrm{p}}^{\mathrm{RPA}}(q)} \right]^{-1} \mathrm{Im}[\varepsilon_{\mathrm{ion}}(q, \omega_{\mathrm{p}}^{\mathrm{RPA}}(q)]. \tag{3.13}$$

The derivative of $\mathrm{Re}[\varepsilon_{\mathrm{eg}}(q,\omega)]$ can be expanded to the second order in q [51]:

$$\left[\left. \frac{\partial \mathrm{Re}[\varepsilon_{\mathrm{L}}(q,\omega)]}{\partial\omega} \right|_{\omega=\omega_{\mathrm{p}}^{\mathrm{RPA}}(q)} \right]^{-1} \approx \frac{1}{2}\left(\omega_{\mathrm{p}} - \frac{3E_{\mathrm{F}}}{5m\omega_{\mathrm{p}}} q^2\right). \tag{3.14}$$

In the calculation of $\hbar\omega_{\mathrm{p}}^{\mathrm{ion}}(0)$ and $\Delta E_{1/2}^{\mathrm{ion}}(q)$, we used the experimentally obtained $S(q)$ [6, 54, 55] and the Ashcroft's empty core potential [56] (The core radius is set to be 1.38 Å [57]).

3.4 Results

3.4.1 Data Analysis

Figure 3.5(a) shows an IXS spectrum of liquid Rb at 773 K, which was scanned at $q = 0.45$ Å^{-1}. A sharp peak of elastic scattering was observed. Figure 3.5(b) shows an enlargement of the spectra in the energy range of 13.836 –13.842 keV. A plasmon excitation peak was observed around at 13.838 keV.

We fitted the elastic peak by the following Gaussian:

$$I_{\mathrm{ela}}(E) = A\exp\left[-\left(\frac{E-E_0}{w}\right)^2\right] + I_0. \tag{3.15}$$

The energy and FWHM of the incident X-ray corresponds to E_0 and $2\sqrt{\ln 2}w$, respectively. In order to determine the plasmon excitation energy, we calculated the energy shift $E - E_0$, where E is the energy of the scattered X-ray.

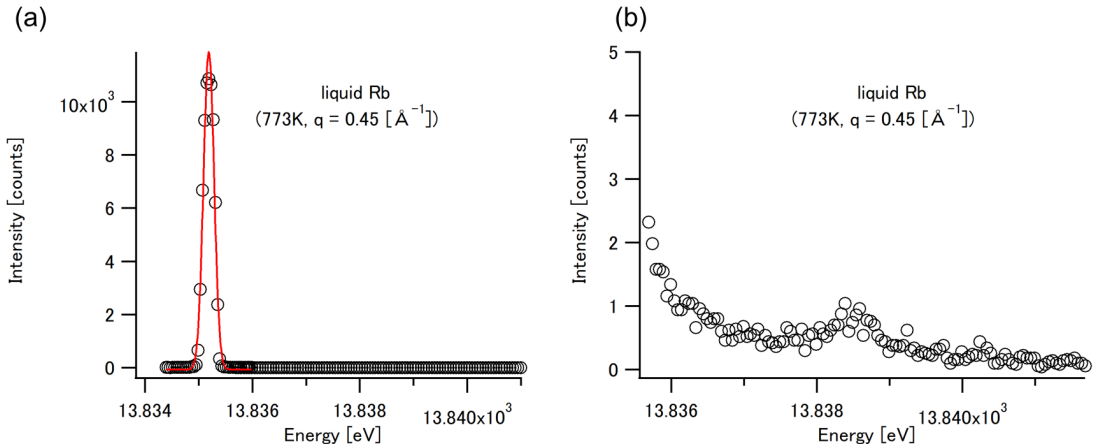

Figure 3.5: (a) IXS spectrum of liquid Rb at 773 K. Solid line represents the Gaussian fitting. (b) Enlargement of the IXS spectrum in the energy range of 13.836 –13.842 keV.

3.4.2 IXS Spectra

Figure 3.6(a) and (b) show the IXS spectra of liquid Rb at 573 and 773 K, where the horizontal axis is the energy shift. Clear peaks due to plasmon are observed at around 3.3 eV. Large scattering intensity appearing below 1 eV represents the elastic scattering. To determine the plasmon energy and line width, we fitted the plasmon peaks using the following model function.

$$I_{\mathrm{pl}}(E) = A \cdot \frac{g_1}{\pi[E^2 + g_1^2]} + B \cdot \frac{g_2}{\pi[(E - E_p)^2 + g_2^2]} + C \tag{3.16}$$

The first and second term corresponds to the inelastic (plasmon) and the elastic contribution, respectively. The energy resolution of 0.22 eV is not negligible compared with the plasmon line width. Thus, the model function was convolved with the Gaussian, the FWHM of which was set to the experimental resolution (0.22 eV). The solid curves in Fig. 3.6(a) and (b) represent the fitting results. The peak position (E_p) and FWHM ($2g_2$) give the plasmon energy and plasmon line width, respectively.

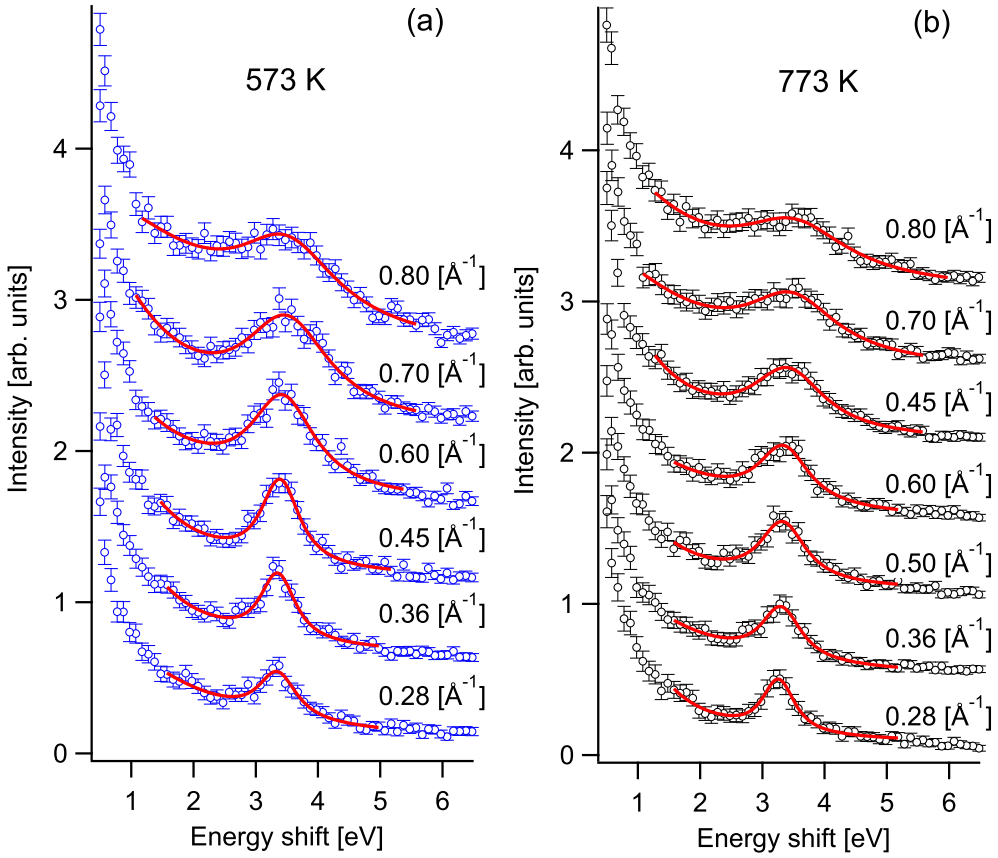

Figure 3.6: IXS spectra of liquid Rb (a) at 573 K and (b) 773 K. The solid curves represent the fits to the plasmon peak.

3.5 Discussion

3.5.1 Plasmon Energy

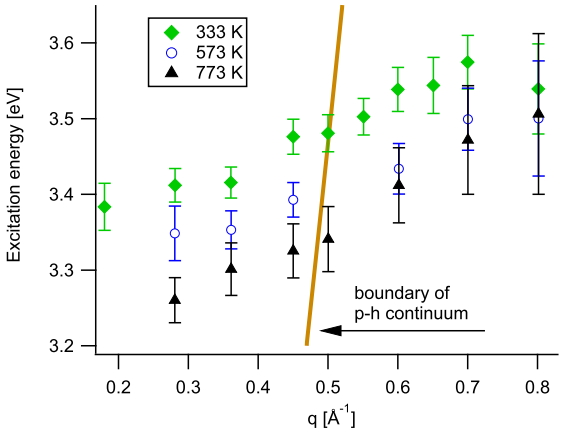

Figure 3.7: Plasmon energy dispersion of liquid Rb at 333, 573, and 773 K. The data at 333 K are taken from the previous IXS measurements [44]. The thick line represents the boundary of the p-h continuum. We calculated the boundary using the density of the liquid Rb at 573 K, and the cutoff wave vector q_c is estimated to be 0.5 Å^{-1} from the intersection of the dispersion and the boundary.

Figure 3.7 shows the dispersion relations of the plasmon energy, determined by the fitting procedure. The results at 333 K, taken from IXS study [44], are also shown in this figure. The plasmon energy at 573 K and 773 K increases with q, positive dispersion, and this tendency agrees with that at 333 K. In low q region ($q < 0.6$ Å^{-1}), the plasmon energy decreases with increasing temperature.

We have calculated the plasmon energy in the electron gas model and made a comparison with the experimental results. The detailed procedure for the calculation is given in Sec. 3.2. The experimentally obtained plasmon energy $\hbar\omega_{\rm p}^{\rm exp}(q)$ and that of the electron gas with the XC effect $\hbar\omega_{\rm p}^{\rm eg}(q)$ are compared in Fig. 3.8(a) and (b). The calculated results reproduce the experimental q dependence of the positive dispersion, however, $\hbar\omega_{\rm p}^{\rm exp}(q)$ takes a lower value than $\hbar\omega_{\rm p}^{\rm eg}(q)$. The lowering of the plasmon energy relative to the electron gas prediction was also observed in other

simple metals near the melting point [35, 43, 44], and it was explained by the effect of ionic structure. Our results suggest that the effect of ionic structure remains at higher temperatures than the melting point. Moreover, note that difference between $\hbar\omega_{\rm p}^{\rm eg}(q)$ and $\hbar\omega_{\rm p}^{\rm exp}(q)$ becomes smaller with increasing temperature. This trend is clearly visible in Figure 3.9, where we plotted $\hbar\omega_{\rm p}^{\rm eg}(q) - \hbar\omega_{\rm p}^{\rm exp}(q)$.

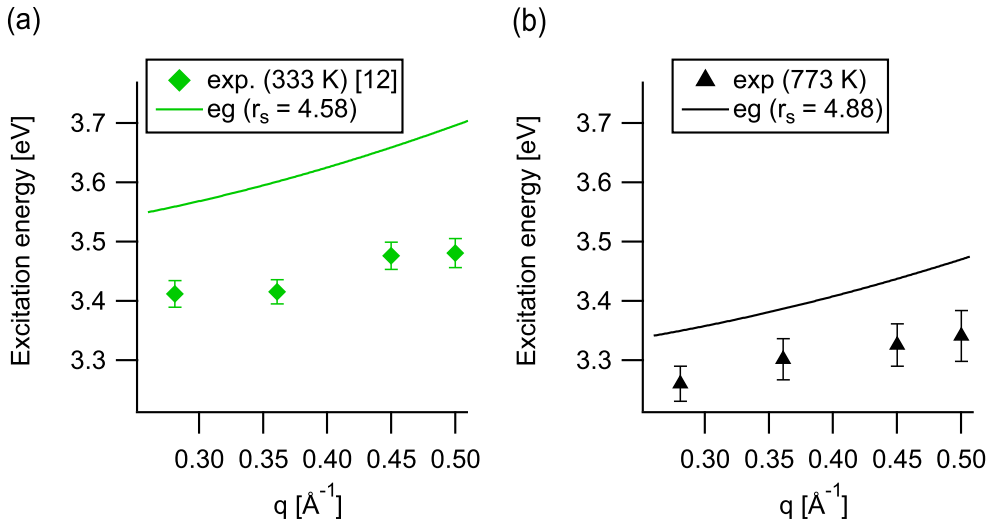

Figure 3.8: (a) and (b) Experimentally obtained plasmon energy at two temperatures and that of the electron gas model.

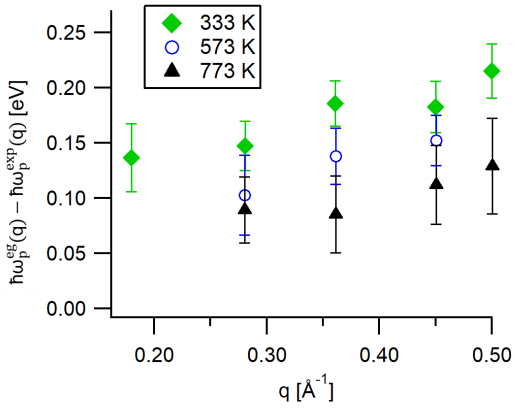

Figure 3.9: Difference between the experimentally obtained plasmon energy $\hbar\omega_{\rm p}^{\rm exp}(q)$ and that of the electron gas model $\hbar\omega_{\rm p}^{\rm eg}(q)$ including the XC effect.

Table 3.1: Temperature (T), fluid density (d) and the calculated plasmon energies at $q = 0$. For the calculation of $\hbar\omega_{\rm p}^{\rm ion}(0)$, we used the experimentally obtained $S(q)$ [6, 54, 55]. The units are eV for $\hbar\omega_{\rm p}^{\rm eg}(0)$ and $\hbar\omega_{\rm p}^{\rm ion}(0)$.

T (K)	d (g/cm^3)	$\hbar\omega_{\rm p}^{\rm eg}(0)$	$\hbar\omega_{\rm p}^{\rm ion}(0)$	$\hbar\omega_{\rm p}^{\rm eg}(0) - \hbar\omega_{\rm p}^{\rm ion}(0)$
350 [54]	1.46	3.479	3.398 ± 0.003	0.081 ± 0.003
373 [55]	1.448	3.466	3.383 ± 0.002	0.083 ± 0.002
473 [55]	1.397	3.414	3.331 ± 0.002	0.083 ± 0.002
573 [6]	1.43	3.448	3.377 ± 0.001	0.071 ± 0.001
773 [6]	1.35	3.364	3.298 ± 0.001	0.066 ± 0.001
900 [54]	1.214	3.212	3.15 ± 0.001	0.062 ± 0.001

To investigate the effect of ionic structure on the plasmon energy, we have calculated the plasmon energy at $q = 0$ including the effect of ionic structure $\hbar\omega_{\rm p}^{\rm ion}(0)$, based on Eq. (3.8) derived in Sec. 3.3.1. In the calculation of the plasmon energy at $q = 0$, it is unnecessary to consider the XC effect, because the XC effect on the plamon energy vanishes at $q = 0$ as obvious from Eq. (3.4). Table 3.1 shows the calculated results, where the plasmon energy in the electron gas model are also calculated for comparison. $\hbar\omega_{\rm p}^{\rm ion}(0)$ is smaller than $\hbar\omega_{\rm p}^{\rm eg}(0)$, which shows that the effect of ionic structure lowers the plasmon energy.

Figure 3.10 shows the density dependence of the plasmon energy. We determined $\hbar\omega_{\rm p}^{\rm exp}(q = 0)$ by fitting the experimental dispersion with $\hbar\omega_{\rm p}^{\rm exp}(q) = \hbar\omega_{\rm p}^{\rm exp}(0) + Aq^2$ in $q < 0.5$ Å^{-1} ($\sim q_{\rm c}$). As seen from Fig. 3.10, $\hbar\omega_{\rm p}^{\rm exp}(0)$ exhibits a similar density dependence to $\hbar\omega_{\rm p}^{\rm eg}(0)$. This observation demonstrates that the density dependence of $\hbar\omega_{\rm p}^{\rm exp}(0)$ is mainly determined by the change in the electron density. However, the value of $\hbar\omega_{\rm p}^{\rm exp}(0)$ is smaller than $\hbar\omega_{\rm p}^{\rm eg}(0)$. If the effect of ionic structure is taken into account [$\hbar\omega_{\rm p}^{\rm ion}(0)$], the calculated results show a good agreement with the experimental results (see open and closed symbols in Fig. 3.10).

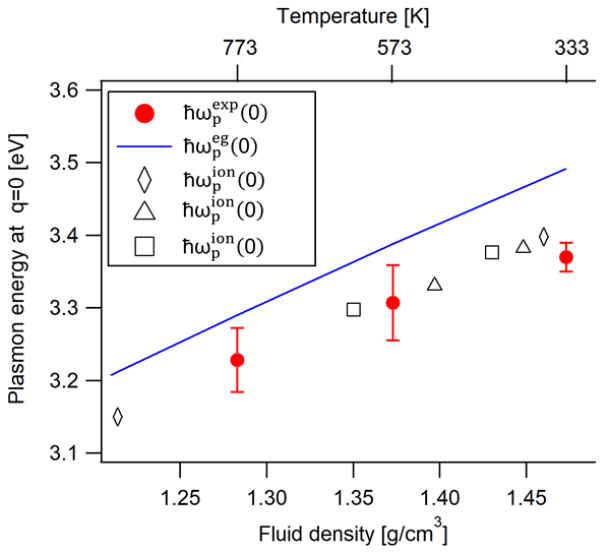

Figure 3.10: Density dependence of the plasmon energy at $q = 0$. The circles corresponds to the experimental results. The open symbols and solid line represent the calculated results of the electron gas model with and without the effect of ionic structure. The error bars of $\hbar\omega_{\rm p}^{\rm ion}(0)$ are smaller than the symbol sizes. The calculated results of $\hbar\omega_{\rm p}^{\rm ion}(0)$ are indicated by different symbols depending on the references of $S(q)$'s used for the calculation (◊ [54], △ [55], □ [6]). The corresponding temperatures of liquid Rb are shown on the upper axis.

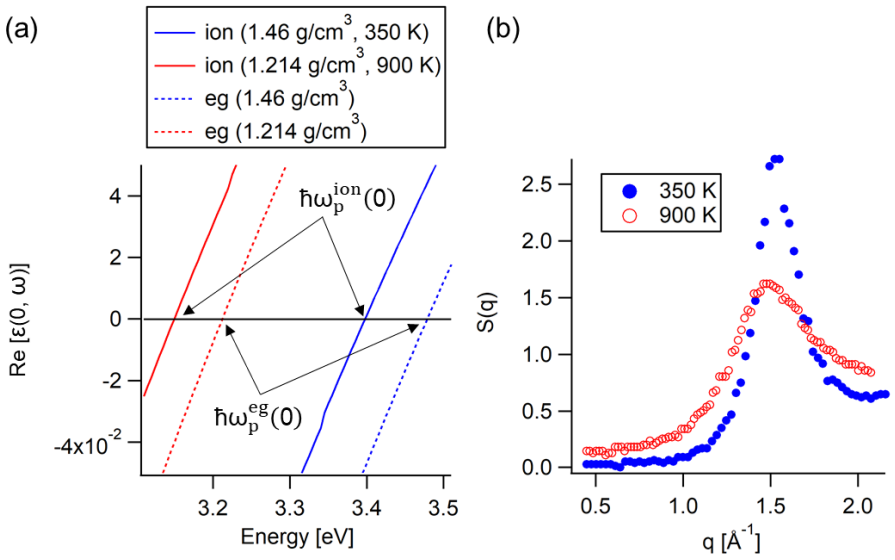

Figure 3.11: (a) Real part of the dielectric function at $q = 0$. The solid lines represent the dielectric function including the effect of ionic structure. The dotted lines represent the dielectric function of the electron gas model. The arrows mark the plasmon energy. The density and temperature used for the calculation are indicated in the legend. (b) Experimentally obtained liquid structure factor of Rb [54]. The data are plotted in the integration interval of Eq. (3.8).

As explained in Sec. 3.3.1, the plasmon energy is determined by the condition $\mathrm{Re}[\varepsilon(0,\omega)]= 0$. Figure 3.11(a) shows $\mathrm{Re}[\varepsilon(0,\omega)]$ for the electron gas model with and without the effect of ionic structure at two temperatures. At a given energy, the $\mathrm{Re}[\varepsilon(0,\omega)]$ including the effect of ionic structure is large relative to that of the electron gas model. Due to this difference of $\mathrm{Re}[\varepsilon(0,\omega)]$, the value of $\hbar\omega_{\mathrm{p}}^{\mathrm{ion}}(0)$ is lower than $\hbar\omega_{\mathrm{p}}^{\mathrm{eg}}(0)$. In $\mathrm{Re}[\varepsilon(0,\omega)]$, the effect of ionic structure is expressed by a term that includes $S(q)$. This term reflects the scattering of plasmons by the ionic potential, because the scattering rate is proportional to $S(q)\,|v_{\mathrm{ion}}(q)|^2$.

We find that the difference between $\hbar\omega_{\mathrm{p}}^{\mathrm{eg}}(0)$ and $\hbar\omega_{\mathrm{p}}^{\mathrm{ion}}(0)$ becomes small with increasing temperature, as can be seen from Table 3.1 $[\hbar\omega_{\mathrm{p}}^{\mathrm{eg}}(0)-\hbar\omega_{\mathrm{p}}^{\mathrm{ion}}(0)]$. Moreover,

we investigated the relation between $S(q)$ and $\hbar\omega_{\rm p}^{\rm eg}(0) - \hbar\omega_{\rm p}^{\rm ion}(0)$ in detail, and this energy difference is found to be correlated with the shape of $S(q)$ of liquid Rb. Figure 3.11(b) shows $S(q)$'s used in the calculation. $S(q)$ has the main peak at around $q = 1.5$ Å^{-1}, and the peak becomes broader with increasing temperature, reflecting the reduced spatial correlation. We have also carried out test calculations using $S(q)$'s with several different peak heights to estimate the effects of the shape of $S(q)$, and found that $S(q)$ with a lower peak height tends to give a smaller value of the last term in ${\rm Re}[\varepsilon^{\rm ion}(0,\omega)]$. Thus, the lowering of the peak height of $S(q)$ is considered to be responsible for the observed trend of $\hbar\omega_{\rm p}^{\rm eg}(0) - \hbar\omega_{\rm p}^{\rm ion}(0)$ presented in Table 3.1. This means that the plasmon energy of the high-temperature liquid, where the ionic structure is thermally disordered, approaches that of the electron gas model.

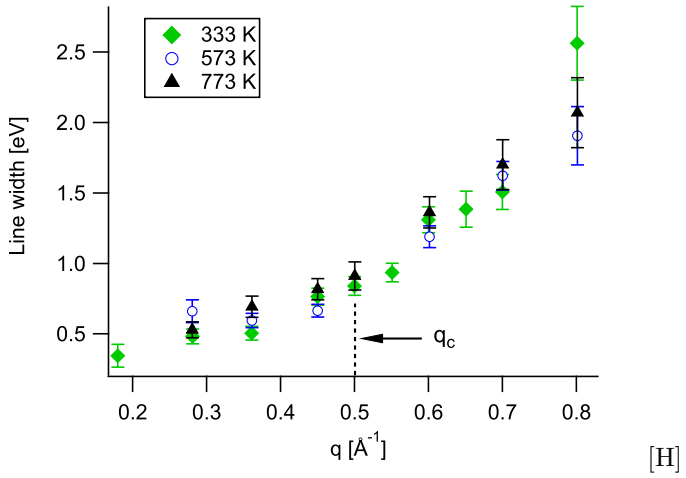

Figure 3.12: (Color online) Plasmon line width of liquid Rb as a function of q. The line width at 333 K is the result of our previous IXS measurements [44].

3.5.2 Plasmon Line Width

Figure 3.12 shows the experimentally determined plasmon line width $\Delta E_{1/2}^{\rm exp}(q)$, which was obtained by the fitting procedure. At 573 and 773 K, the plasmon line width increases with q. This trend qualitatively agrees with the previous results near the melting point [44]. In $q > q_{\rm c}$, the line width increases with q faster than in $q < q_{\rm c}$, which indicates that the plasmon strongly damps in the p-h continuum. Regarding the temperature dependence, the results are so scattered that the identification of a systematic temperature trend is difficult. Thus, we focus on the discussion of the q dependence of the plasmon line width.

We performed the calculation of the plasmon line width to investigate the origin of the plasmon damping in liquid Rb. The plasmon line width is mainly affected by three effects, i.e., interband transition induced by the ionic potential, the XC effect, and intraband (or interband) transitions assisted by phonons [46, 51]. (i) The plasmon line width due to interband transition is described by using a pseudopotential and $S(q)$ as described in Sec. 3.3.2. (ii) The plasmon line width due to the XC

effect is caused by the interaction of the plasmon with multiple p-h pair excitations, which is a many-body effect beyond the RPA [58]. (iii) In the case of liquid metals, the dynamic scattering effect by thermal ionic motion is negligible for describing the electrical resistivity [59]. Hence, we neglect the effect of phonon on the plasmon line width. In fact, the phonon contribution of the line width, estimated from the electrical resistivity, gives a minor contribution compared to that due to interband transition by the ionic potential [46]. We express the plasmon line width in the liquid as the sum of the effect of ionic structure and the XC effect:

$$\Delta E_{1/2}^{\mathrm{calc}}(q) = \Delta E_{1/2}^{\mathrm{ion}}(q) + \Delta E_{1/2}^{\mathrm{xc}}(q). \tag{3.17}$$

An expression of $\Delta E_{1/2}^{\mathrm{ion}}(q)$ at finite q has been derived in Sec. 3.3.2. Acording to the electron gas model, $\Delta E_{1/2}^{\mathrm{xc}}(q)$ is described by the exchange-correlation kernel $f_{\mathrm{xc}}(\omega)$ [58]

$$\Delta E_{1/2}^{\mathrm{xc}}(q) \approx -\frac{\hbar n q^2}{m_{\mathrm{b}}\omega_{\mathrm{p}}^{\mathrm{eg}}(0)}\mathrm{Im} f_{\mathrm{xc}}(\omega_{\mathrm{p}}^{\mathrm{eg}}(0)). \tag{3.18}$$

In the calculation of $\Delta E_{1/2}^{\mathrm{xc}}(q)$, we used the exchange-correlation kernel calculated by Qian and Vignale [60], which only depends on r_{s}.

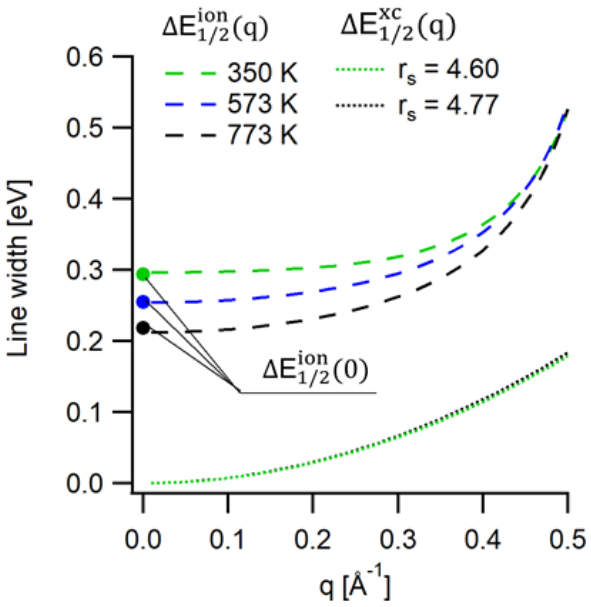

Figure 3.13: q dependence of the calculated plasmon line width. The dashed lines correspond to $\Delta E^{\rm ion}_{1/2}(q)$, and the dotted line represents $\Delta E^{\rm xc}_{1/2}(q)$, where $r_{\rm s} = 4.60$ and $r_{\rm s} = 4.77$ correspond to the electron density of liquid Rb at 350 and 773 K, respectively. The circles show $\Delta E^{\rm ion}_{1/2}(0)$, which is calculated from Eq. (3.5).

Figure 3.13 shows the calculated plasmon line width for $q < q_{\rm c}$ (~ 0.5 Å^{-1}). $\Delta E^{\rm ion}_{1/2}(q)$ calculated from Eq. (3.13) smoothly connects to $\Delta E^{\rm ion}_{1/2}(q = 0)$ calculated from Eq. (3.5). Thus, the formula derived in this work is consistent with those of our previous work [46]. As for the temperature dependence, $\Delta E^{\rm ion}_{1/2}(q)$ becomes small as the temperature increases. This temperature dependence is caused by the change in $S(q)$ as in the case of $\hbar\omega^{\rm ion}_{\rm p}(0)$. On the other hand, there is only a small difference between $\Delta E^{\rm xc}_{1/2}(q)$ at $r_{\rm s} = 4.60$ and $r_{\rm s} = 4.77$, and the density dependence $\Delta E^{\rm xc}_{1/2}(q)$ is very weak.

Figure 3.14 shows and the experimental and the calculated results. The value of $\Delta E^{\rm xc}_{1/2}(q)$ is much smaller than that of $\Delta E^{\rm exp}_{1/2}(q)$, and only the XC effect is insufficient to explain the experimental results. However, when the effect of ionic structure is

included, the agreement is greatly improved [see $\Delta E_{1/2}^{\rm cal}(q)$ and $\Delta E_{1/2}^{\rm exp}(q)$]. This observation shows the importance of the ionic structure to describe the plasmon lifetime in liquid Rb.

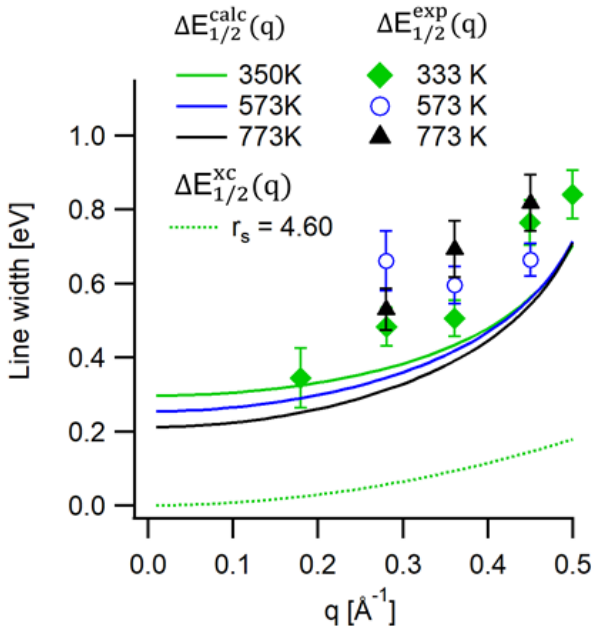

Figure 3.14: Comparison of $\Delta E_{1/2}^{\rm exp}(q)$ with $\Delta E_{1/2}^{\rm calc}(q)$ at three temperatures. $\Delta E_{1/2}^{\rm xc}(q)$ at $r_{\rm s} = 4.60$ is also shown by the dotted line. The temperatures in the legends [$\Delta E_{1/2}^{\rm ion}(q)$ and $\Delta E_{1/2}^{\rm cal}(q)$] represent that of $S(q)$ used for the calculation (350 [54], 573, and 773 K [6]).

3.6 Summary

We have experimentally determined the plasmon energy and line width in liquid Rb at high temperatures beyond the melting point. The observed plasmon energy becomes smaller with increasing temperature, which reflects the variation of the electron density. This density dependence is qualitatively consistent with the prediction of the electron gas model, however, the absolute value is lower than this prediction. We have calculated the plasmon energy of liquid Rb at $q = 0$ which takes into account the effect of ionic structure, and the calculated results well reproduced the experimental results. Moreover, the theoretical calculations show that the effect of ionic structure on the plasmon energy becomes weaker with increasing temperature, reflecting the reduced spatial correlation of the ions.

We have calculated the plasmon line width of liquid metals at finite q. The agreement between the calculated and the experimental results is improved if the effect of ionic structure is included. These results suggest that the effect of ionic structure is essential for plasmons in high-temperature liquid metals.

For fluid Rb in lower density state, a spatial inhomogeneity of the electron and ion was observed [6–9]. In such region, the structural inhomogeneity could affect the plasmon behavior, and the obtained information on the effect of ionic structure would be useful. We found that the temperature dependence of plasmon energy in the liquid is mainly ruled by the electron density. Thus, the experimental determination of the plasmon energy in the lower density state offers valuable information on the electronic charge density in fluid Rb.

Chapter 4

Static Density Response Function of Li: $2k_F$ Singularity

4.1 Introduction to This Chapter

Dielectric screening is an important concept for describing the effective interaction in electron gas, which is formulated by the linear response theory [11]. The static screening electron density $\Delta n(q)$ induced by external potential $V_{\rm ext}(q)$ is described by the static density response function $\chi(q,0)$:

$$\Delta n(q) = V_{\rm ext}(q)\chi(q,0). \tag{4.1}$$

A representative example of the density response function is provided by the electron gas model within the RPA [11, 47]:

$$\chi^{\rm RPA}(q,0) = \chi_0(q,0)\left[1 - \frac{4\pi e^2}{q^2}\chi_0(q,0)\right]^{-1}. \tag{4.2}$$

Here $\chi_0(q,0)$ is the density response function of independent particle, and it describes the response to effective potential as $\Delta n(q) = V_{\rm eff}(q)\chi_0(q,0)$. Figure shows the RPA

density response function, which is calculated with $r_s = 4.0$. The response function is continuous at $q = 2k_F$, however, its derivative shows a logarithmic singularity ($2k_F$ singularity). This singularity reflects the sharp cutoff in the momentum distribution, and it is the origin of spatially oscillating screening electron density in metals, the so called Friedel oscillation [61]. The many-body effects beyond the RPA on the density response function can be included with the local field correction $G(q)$ [11]:

$$\chi^{\mathrm{XC}}(q,0) = \chi_0(q,0)\left[1 - \frac{4\pi e^2}{q^2}(1 - G(q))\chi_0(q,0)\right]^{-1}. \tag{4.3}$$

A considerable theoretical effort has been made towards the construction of $G(q)$ with the aim of a deeper understanding of dielectric screening [11, 13, 48].

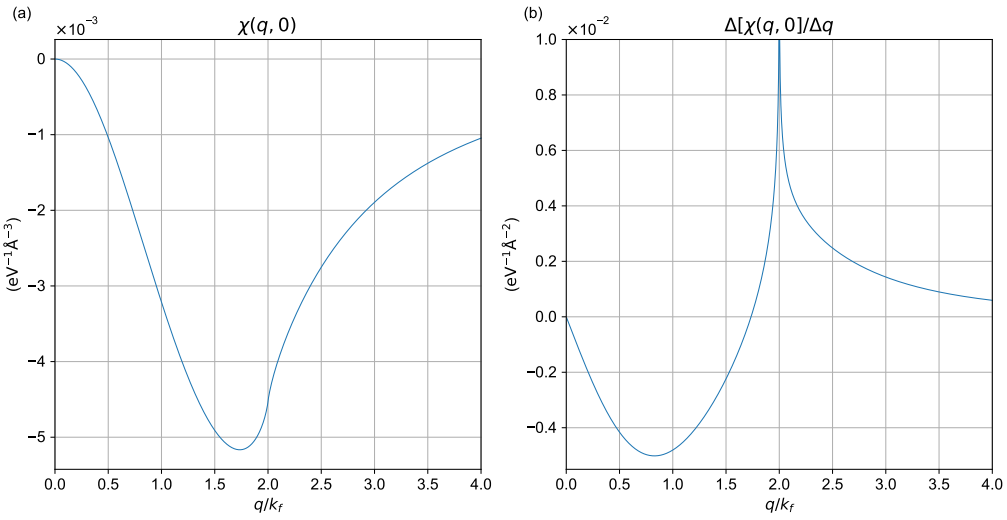

Figure 4.1: (a) Static density response function of the electron gas model within the RPA (Eq. (4.2)). (b) Derivative of the density response function.

Physical quantities that reflect dielectric screening in metals have been extensively measured. The standing waves which are related to Friedel oscillations were obtained by scanning tunneling microscopy [62, 63]. In principle, the screening electron den-

sity can be reconstructed from the measured standing waves [58, 64], however, the reconstruction with a scanning tunneling microscope has not been achieved to our knowledge. In the field of liquid metals, effective interionic potential was determined from the experimentally determined liquid structure factor using the statistical theory of liquids [65, 66]. The effective interionic potential $\phi(\boldsymbol{r})$ is related to $\chi(q,0)$ via the following relation [67]:

$$\phi(\boldsymbol{r}) = \frac{(Ze)^2}{r} + \int \frac{d\boldsymbol{q}}{(2\pi)^3}\chi(q,0)|v_{\rm ion}(\boldsymbol{q})|^2 \exp(i\boldsymbol{q}\cdot\boldsymbol{r}), \tag{4.4}$$

where $v_{\rm ion}(\boldsymbol{q})$ is the pseudopotential. The first and the second term represent the bare ion-ion interaction and the induced contribution by the screening electrons. It is well known that the experimentally determined $\phi(\boldsymbol{r})$ exhibits $2k_F$ oscillations in liquid states [68]. Indirect information on screening can be obtained through the effective interionic potential, however, this approach does not provide $\chi(q,0)$, which is a key quantity for describing dielectric screening.

There are several spectroscopy methods to determine the density response function or dielectric function. Figure 4.2 illustrates region where each experimental method can be applied to determine the density response function or dielectric function. The ω dependence of $\varepsilon(q \approx 0, \omega)$ can be calculated from reflectivity which is obtained by optical measurement. However, the wave vector of visible light is much smaller than the Fermi wave vector, and only the $q \approx 0$ region can be explored with optical measurement [69]. EELS and IXS provide the q dependence of $\mathrm{Im}[\chi(q,\omega)]$. EELS is a powerful tool to investigate the electronic excitation in low q region ($q < 1$ Å^{-1}), but it suffers from multiple scattering effects in high q region [70]. The multiple scattering effects are very small for IXS, and the q dependence of $\mathrm{Im}[\chi(q,\omega)]$ in a wide q range can be obtained by IXS measurement. Basically, these spectroscopy methods give information on dynamic property ($\omega \neq 0$), however, Reed [25] pointed out that the *static* density response function can be constructed from IXS spectra

based on the concepts of causality. Figure 4.3 shows the static screening electron density of graphene calculated from the density response function. The electrons screen the charge impurity in a few nanometers.

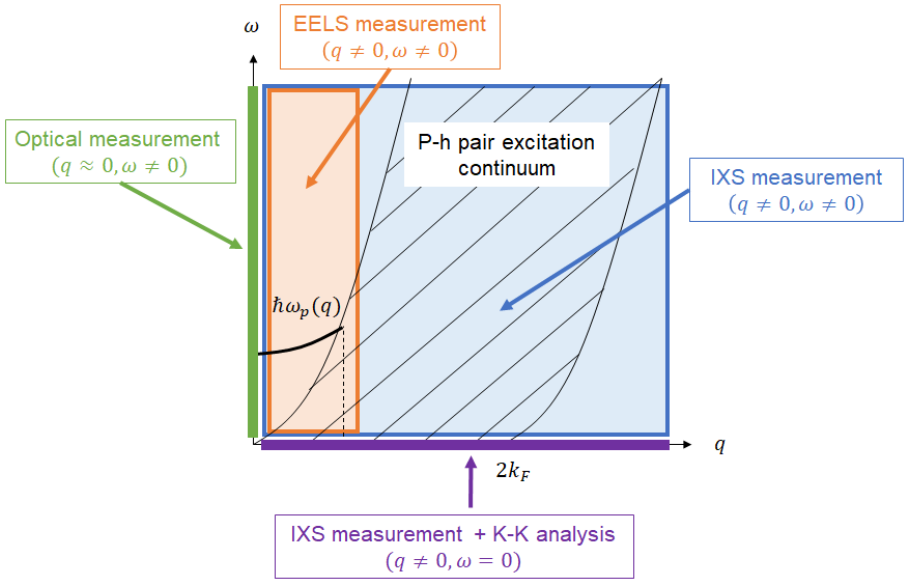

Figure 4.2: Schematic illustration of the region where each spectroscopy method can be applied to investigate the density response function or dielectric function.

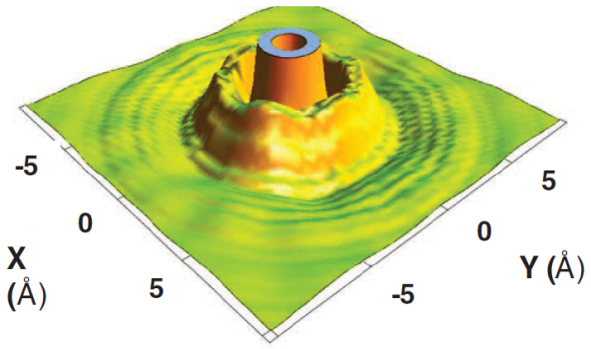

Figure 4.3: Screening electron density induced by a static point charge in graphene. (reprinted from Ref. [25])

The static density response function of a simple metal has not been experimen-

tally determined in spite of its importance in the theory of metals [11]. In this study, we performed IXS experiments on solid and liquid Li to determine $\chi(q,0)$. Li is suited for the investigation of screening in simple metals for the following reasons. (i) The valence electron of Li is well described with the electron gas model. (ii) Strong IXS signals can be obtained because of the small X-ray attenuation of Li. (iii) Extensive knowledge for $S(q,\omega)$ of solid Li has been accumulated [30–35]. Moreover, we compared the results for the solid and the liquid to clarify the effect of disorder on the $2k_F$ singularity. In liquid states, the Fermi surface is smeared owing to the effect of disorder [68,71,72]. The effect of Fermi surface blurring on screening has been theoretically investigated [53, 73, 74], however, experimental information on this effect is sparse.

This chapter is organized as follows. In Sec. 4.2., we show the procedure to derive the dynamic structure factor and the density response function from the raw IXS spectra. In Sec. 4.3, we discuss the q dependence of static density response function. Moreover, we calculate the screening electron density using the response function. Finally in Sec. 4.4, we present the summary of this chapter.

4.2 Results

4.2.1 Raw IXS Spectrum

Figure 4.4 – 4.7 show raw IXS spectra $I(q,E)$ of solid and liquid Li, where E is the energy of the scattered X-ray. The sharp peaks observed around 19980 eV are the contribution of elastic scattering. The inelastic peak of electronic excitations was observed in energy region lower than 19980 eV. In low q region ($0.30 < q < 0.80$ Å^{-1}), the IXS spectra were collected in 19870 – 19990 eV ($-10 < \hbar\omega < 110$ eV). The energy transfer was calculated as $\hbar\omega = E_0 - E$, where E_0 is the energy of the incident X-ray. In high q region ($1.01 < q < 3.47$ Å^{-1}), the IXS spectra were

collected in 19630 – 19990 eV ($-10 < \hbar\omega < 350$ eV). The inelastic peaks in high q were observed at higher energies than in low q, and the energy scan in high q was carried out in a wide energy range.

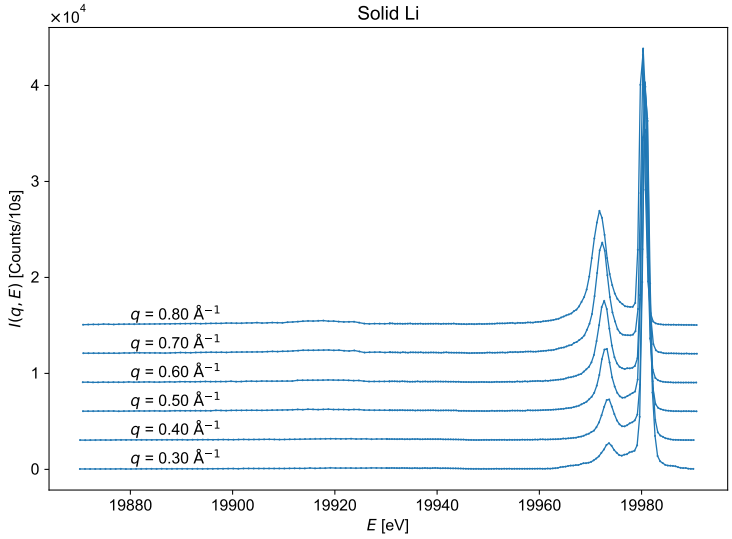

Figure 4.4: IXS spectra of solid Li in $0.3 < q < 0.8$ Å^{-1}.

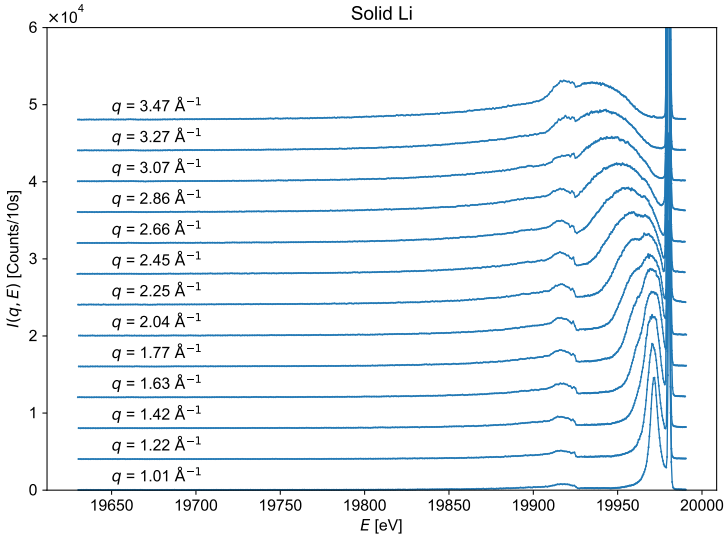

Figure 4.5: IXS spectra of solid Li in $1.0 < q < 3.5$ Å^{-1}.

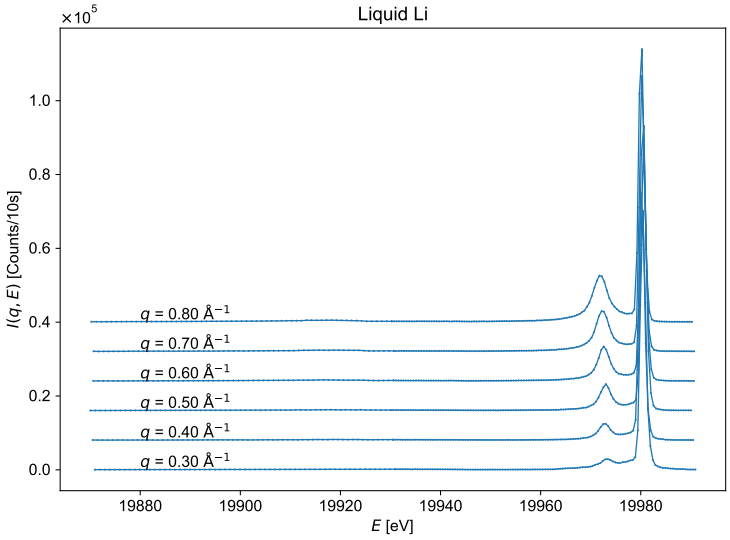

Figure 4.6: IXS spectra of liquid Li in $0.3 < q < 0.8$ Å^{-1}.

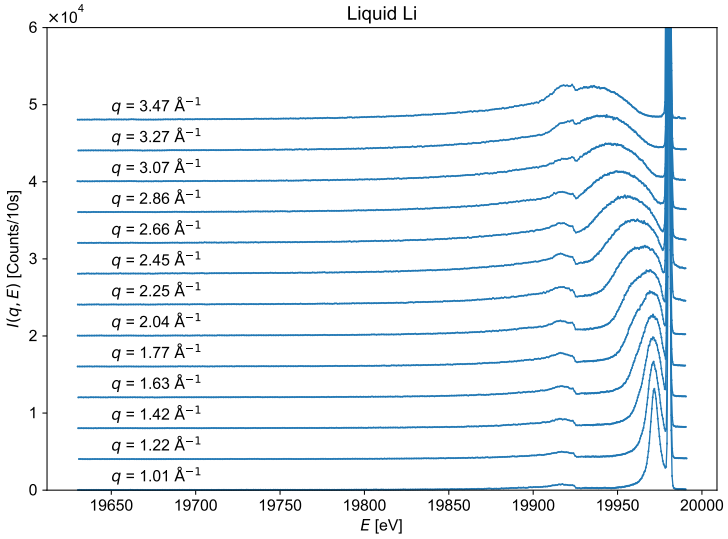

Figure 4.7: IXS spectra of liquid Li in $1.0 < q < 3.5$ Å^{-1}.

4.2.2 Data Analysis

Subtraction of the Elastic Scattering and Extrapolation of the Spectra

In this section, we derive the IXS spectra of electronic excitations by following procedure. (i) We determined the energy of the incident X-ray in the same way as in Sec 3.4.1. (ii) We subtracted the signal of the background from that of the sample. (iii) The elastic component consists of ionic contributions, and we removed this component to obtain the IXS spectra of electronic excitations. As seen in Fig. 4.8, the elastic component was subtracted by the Voigt fitting. (iv) The subtracted spectra were extrapolated to 0 eV using a model function so that $I(q, \omega) = 0$ at $\omega = 0$. We used a linear function or the density response function of Mermin [75] as a model function, and Figure 4.9(a) and (b) show the extrapolated spectra. The analytic expression for Mermin's function is presented in the Appendix B.2. Since the difference in extrapolation methods influenced the results of the K–K transformation,

we show the results of both methods in the following section. (v) The spectra in $0.30 < q < 0.80$ Å^{-1} were extrapolated to 350 eV by Lorentzian fit so that the energy range in $0.30 < q < 0.80$ Å^{-1} is same as in $1.01 < q < 3.47$ Å^{-1}.

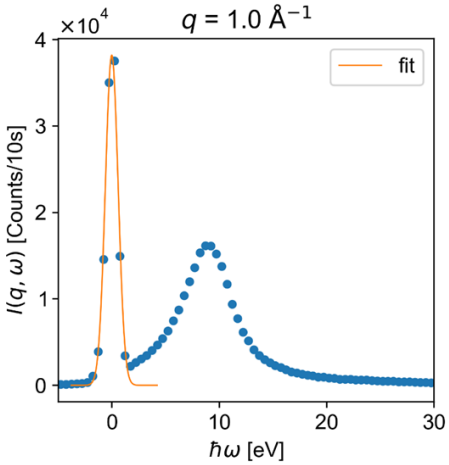

Figure 4.8: Fitting of the elastic component of solid Li at $q = 1.0$ Å^{-1}.

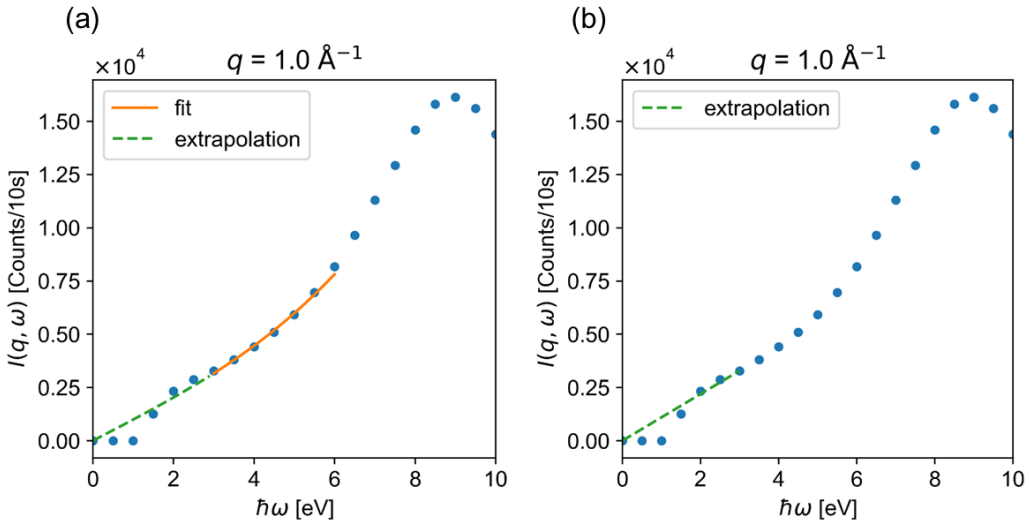

Figure 4.9: (a) Energy extrapolation of the IXS spectrum which is performed by the density response function of Mermin. (b) Energy extrapolation by linear function.

Normalization of IXS Spectra

In this section, we normalized the IXS spectra to obtain $S(q, \omega)$. First, we corrected the spectra by the polarization factor $P(\theta)$. The X-ray was linearly polarized in the horizontal plane of the synchrotron, and the polarization factor is expressed as $P(\theta) = \cos^2 2\theta$. Then, the extrapolated spectra was normalized with the valence electron density n using the *f*-sum rule [16]:

$$\int_0^\infty d\omega S(q, \omega)\omega = \frac{nq^2}{2m}. \tag{4.5}$$

However, the integration over the whole range did not provide an accurate absolute scale, because the IXS spectra in the energy range higher than 55 eV included the core electron excitations contribution (See Fig. 4.10). To normalize the spectra only with the valence contribution, we terminated the integration at 55 eV. Figure 4.11 shows the sum rule integral at each q. The q dependence of the integral is well described by a q^2 power law, except in high q range. The deviation in high q range is due to the underestimation of the sum integral. The valence electron spectra shifts to higher energies with increasing q and gradually merges with the core electron spectra in $\hbar\omega > 55$ eV. Therefore, we determined the absolute scale by fitting the *f*-sum integral in $q < 1.63$ Å^{-1}, where the q^2 power law is satisfied.

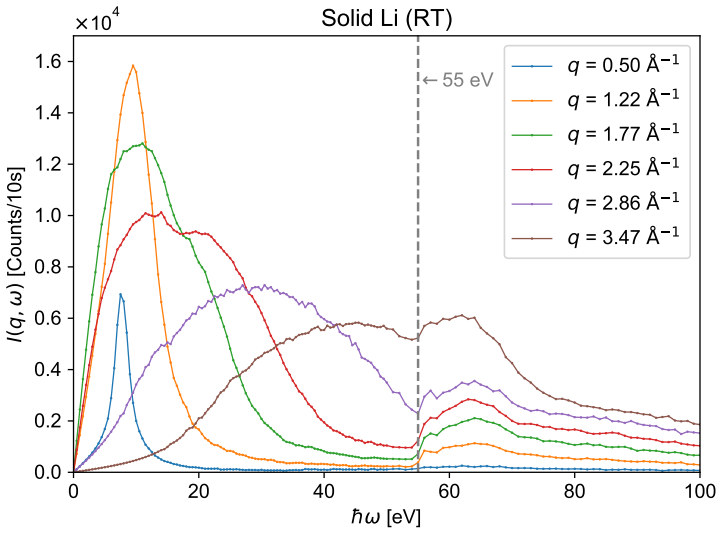

Figure 4.10: The IXS spectra of solid Li at various q. The dashed line indicates the position of the K-edge.

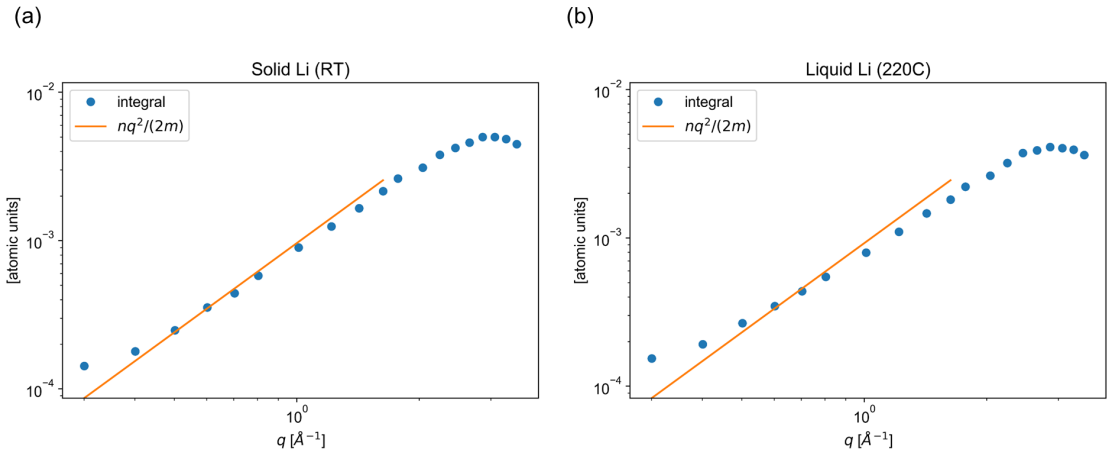

Figure 4.11: Sum rule integral of (a) solid Li and (b) liquid Li.

4.3 Discussion

4.3.1 Dynamic Structure Factor

Figure 4.12 and 4.13 show the experimentally determined $S(q, \omega)$. In the low q range ($q < q_c$), a sharp peak of a plasmon is observed, where q_c is estimated to be 0.9 Å^{-1} using the electron gas model [51]. In the high q range ($q > q_c$), the spectra are dominated by a broad feature of p-h pair excitations. In addition to the contribution of core electron excitations, the K-edge structure is observed at around 55 eV, and its intensity increases with q.

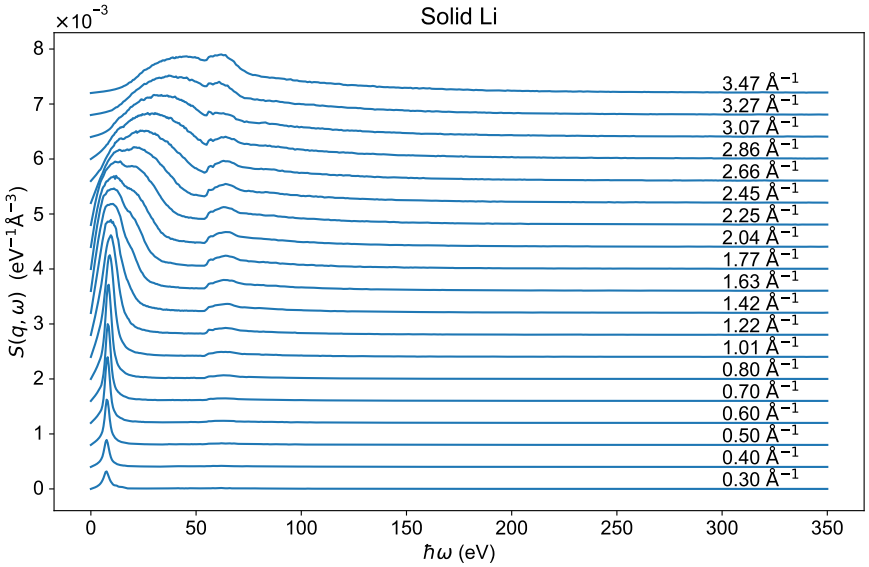

Figure 4.12: Dynamic structure factor in solid Li.

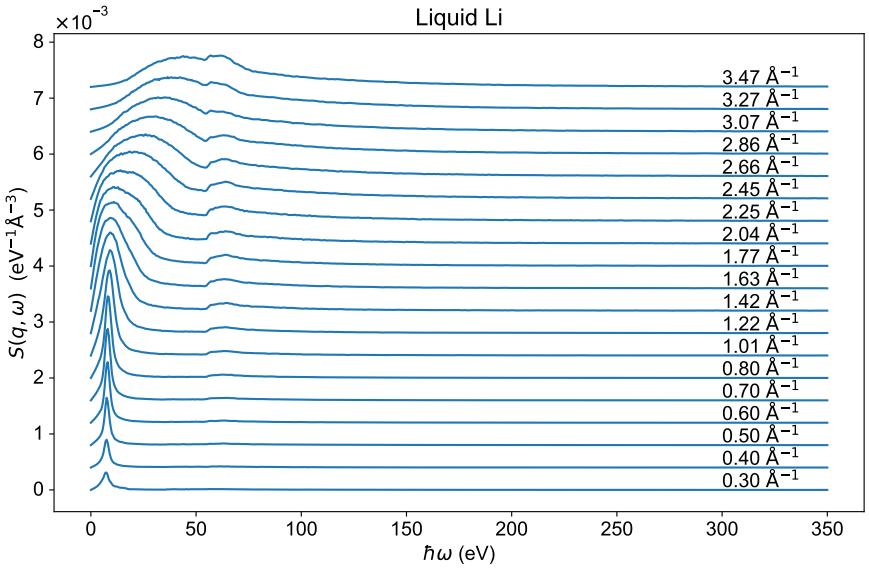

Figure 4.13: Dynamic structure factor in liquid Li.

We determined the plasmon energy and line width by fitting IXS spectra based on the procedure described in Sec. 3.4.2. Figure 4.14 shows the obtained plasmon energy and line width, and the results of previous IXS measurements by Hill *et al.* [35] are also shown for comparison. The experimentally obtained plasmon energy shows a good agreement with that of Hill *et al.*. Regarding the plasmon line width, the errors of our measurements are large, but our results quantitatively reproduces the results of Hill *et al.*.

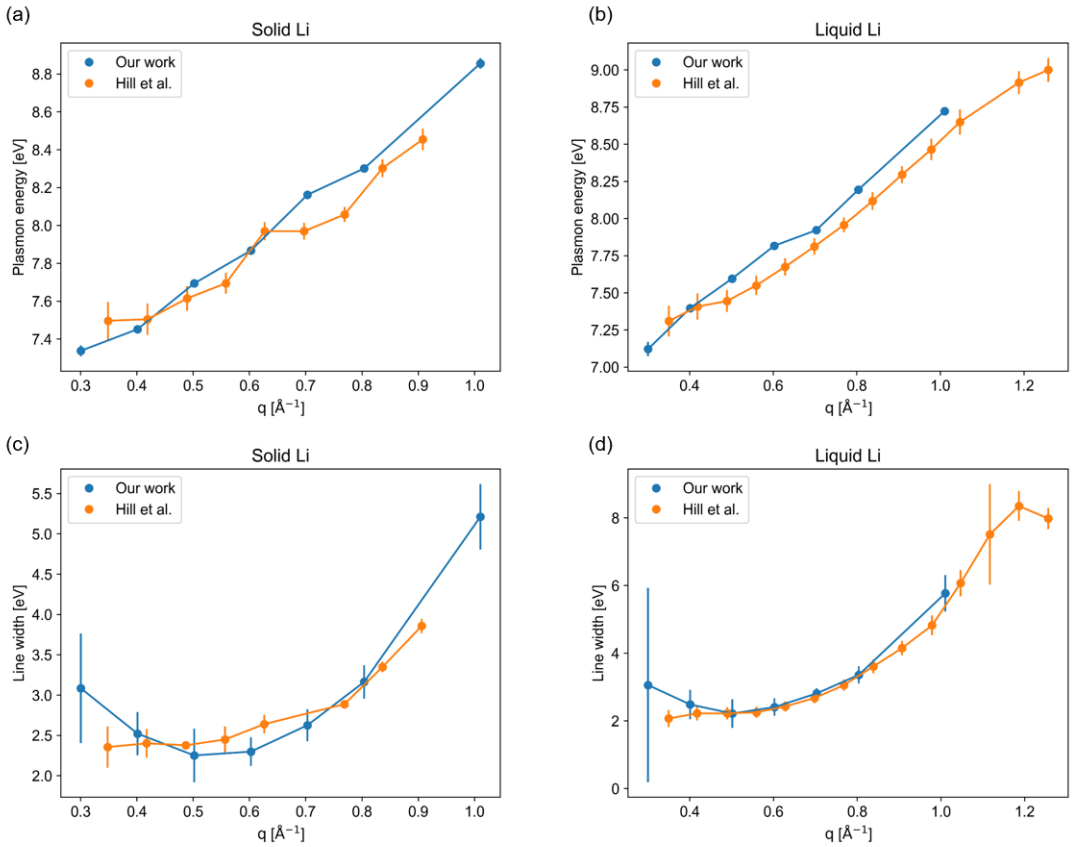

Figure 4.14: Comparison of the plasmon energy with previous IXS measurements by Hill *et al.* [35] in (a) solid Li and (b) liquid Li. The plasmon line width is also compared in (c) and (d).

We compare the experimentally obtained dynamic structure factor with previous IXS measurements of single-crystal Li by Schülke *et al.* [33]. Note that the definition of $S(q,\omega)$ in this paper is slightly different from that of Ref. [33], and they are connected by the following relation:

$$S'(q,\omega) = \frac{S(q,\omega)}{n}, \tag{4.6}$$

where $S'(q,\omega)$ is the dynamic structure factor defined in Ref. [33]. Moreover, the measurement energy range of Ref. [33] is narrower than our measurements, and we

calculated $S'(q,\omega)$ by normalized the IXS spectra in the energy range of Ref. [33]. Figure 4.15 shows the comparison of $S'(q,\omega)$. Although there is a small difference depending on the crystal orientation, our results show a good agreement with the previous measurements.

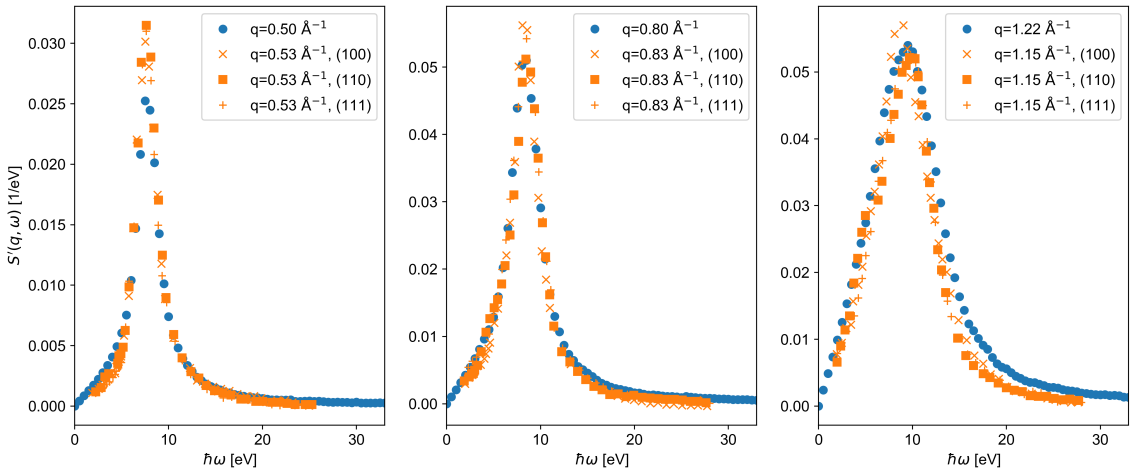

Figure 4.15: Comparison of $S'(q,\omega)$ with previous IXS measurements by Schülke *et al.* [33] at various q. Blue and orange markers represent the data of ours and Ref. [33], respectively. The resolution of the previous measurements is 1.35 eV, which is close to the value of our measurements (1.2 – 1.4 eV).

4.3.2 Imaginary Part of the Density Response Function

We calculated the imaginary part of $\chi(q,\omega)$ from $S(q,\omega)$ based on the fluctuation dissipation theorem (Eq. (1.4)). Figure 4.16 shows a color plot of $-\mathrm{Im}[\chi(q,\omega)]$ for solid Li. In $q < q_c$, the spectra are dominated by a plasmon excitation. In $q > q_c$, the feature of p-h pair excitations and the K-edge was observed. Figure 4.17(a) shows the plasmon spectra of the solid and the liquid. The different energy extrapolation methods are indicated by solid and dashed lines. The plasmon spectrum shows little change on melting. Figure 4.17(b) shows spectra for the solid and the liquid in $q > q_c$. The dip at around 17 eV in the solid spectrum, which is caused by the

band structure effect [35], is blurred on melting.

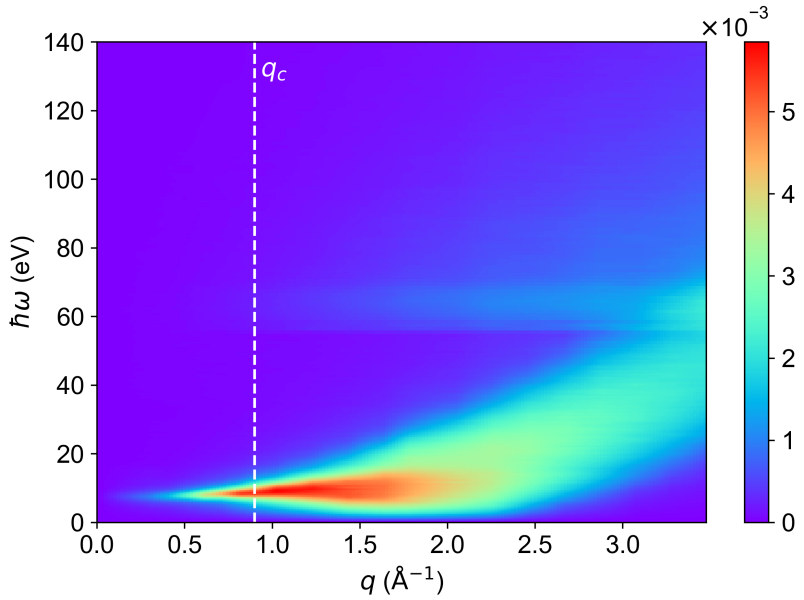

Figure 4.16: Experimentally determined $-\mathrm{Im}\chi(q,\omega)$ of solid Li.

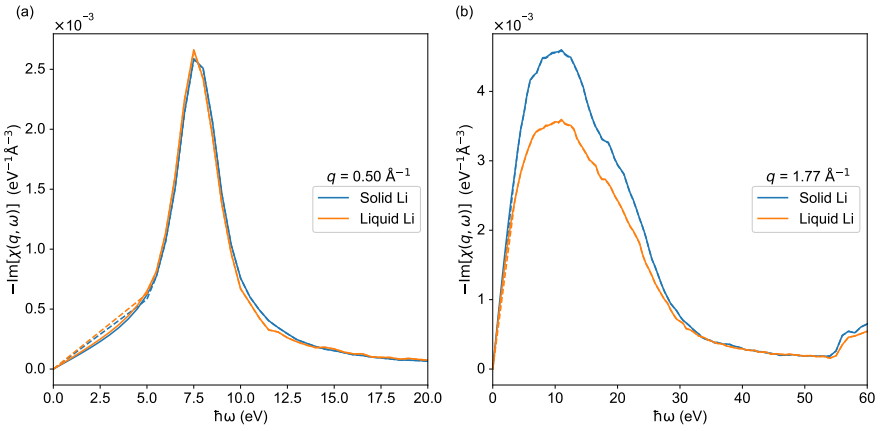

Figure 4.17: (a) $-\mathrm{Im}[\chi(q,\omega)]$ of solid and liquid Li at $q = 0.50$ Å^{-1}. The dashed line indicates the extrapolation to 0 eV using a linear function, and the solid line indicates the extrapolation using the density response function of Mermin. (b) Spectra at $q = 1.77$ Å^{-1}

4.3.3 Static Density Response Function

We derived $\chi(q,0)$ using the K–K relation:

$$\chi(q,0) = \mathrm{Re}[\chi(q,\omega=0)] = \frac{1}{\pi} P \int_{-\infty}^{\infty} d\omega' \frac{\mathrm{Im}[\chi(q,\omega')]}{\omega' - 0}, \tag{4.7}$$

where it is noted that $\chi(q,0)$ is purely real. Figures 4.18(a) and (b) show the experimentally obtained $\chi(q,0)$ for the solid and the liquid. Difference caused by energy extrapolation is small. We calculated $\chi(q,0)$ in the electron gas model within the RPA for comparison with the experimental results. The calculated results were convolved with a Gaussian to take into account the experimental resolution of 0.1 $\mathrm{\AA}^{-1}$. The experimentally determined $\chi(q,0)$ quantitatively reproduced the q dependence of the electron gas results. To investigate the $2k_F$ singularity, we calculated the derivative of $\chi(q,0)$. It is noted that the experimentally determined $\Delta\chi(q,0)/\Delta q$ exhibits a maximum near $2k_F$. The maximum must reflect the logarithmic singularity, which is predicted in the electron gas model. $\chi(q,0)$ of the solid shows very similar q dependence with that of the liquid, however, the derivative near $2k_F$ in the liquid is smaller than in the solid. This trend should be attributed to the blurring of the Fermi surface upon melting, because the $2k_F$ singularity arises from the sharpness of the Fermi surface.

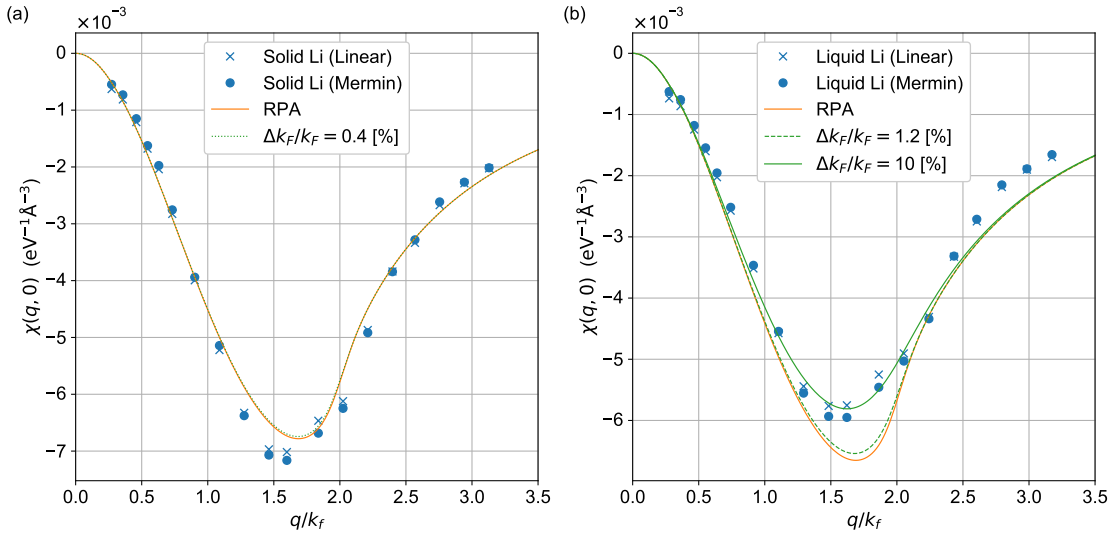

Figure 4.18: (a) Experimentally obtained $\chi(q,0)$ in solid Li and that in the electron gas model. The different energy extrapolation methods are indicated in the legend (Linear or BM). The solid line is the calculated result for the electron gas model within the RPA and the dashed line is that including the effect of Fermi surface blurring. (b) Corresponding results for liquid Li. q is scaled by the Fermi wave vector with $k_F^{\mathrm{Solid}} = 1.11$ Å^{-1} and $k_F^{\mathrm{Liquid}} = 1.09$ Å^{-1}.

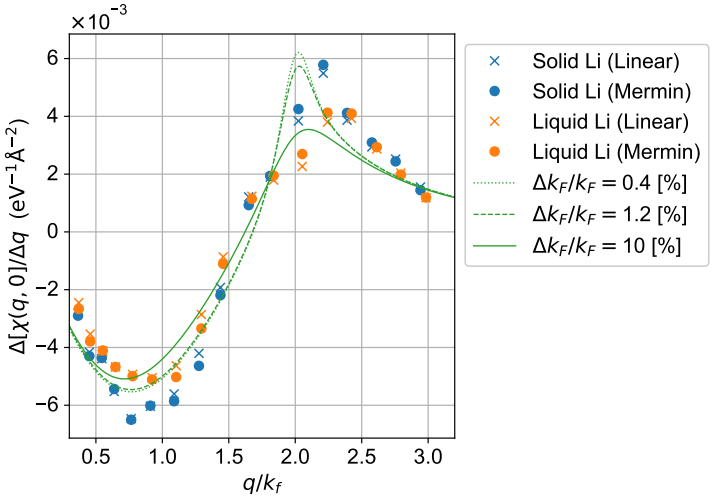

Figure 4.19: Derivative of $[\chi(q,0)]$ for solid and liquid Li. Calculated results with the effect of Fermi surface blurring is also shown.

Table 4.1: Electrical resistivity, mean free path and ratio $\Delta k_F/k_F$.

	$\rho(\Omega \cdot \mathrm{m})$	l (Å)	$\Delta k_F/k_F$ (%)
olid Li	8.55×10^{-8} [56]	115.2	0.4
Liquid Li	26.33×10^{-8} [55]	38.5	1.2
Liquid Li		4.6	10 [76]

To investigate the effect of Fermi surface blurring, we calculated $\Delta\chi(q, 0)$ using the dielectric function $\varepsilon(q, l)$ derived by Leavens *et al.* [74]. Leavens *et al.* expressed the effect of Fermi surface blurring on $\varepsilon(q, l)$ with the mean free path l. Based on the Heisenberg uncertainty principle, the blurring of k_F can be roughly estimated to be $\Delta k_F \sim 1/(2l)$. Δk_F and l, which are estimated from the electrical resistivity, listed in Table 4.1. However, the estimated $\Delta k_F/k_F$ of liquid Li is much smaller than that calculated by the Green function method [1] [76] (See Table 4.1). In liquid metals, the electronic state is strongly affected by the scattering effects of disordered ions, and it is necessary to consider the disordered scattering effect for the estimation of Δk_F. Such effect is taken into account in the calculation by Yan [76] through the self-energy, and Δk_F estimated by the Green function method is more accurate than the estimation using the electrical resistivity. Thus, we also carried out the calculation of $\varepsilon(q, l)$ by setting the parameter l such that Δk_F is equal to the value calculated by Yan [76], and listed the conditions for calculating $\varepsilon(q, l)$ in Table 4.1. The analytic expression and calculated results of $\varepsilon(q, l)$ are presented in Appendix B.3.

Using Eq. (1.5), we calculated $\chi(q, 0)$ from $\varepsilon(q, l)$, and the calculated results are shown in Figs. 4.18(a) and (b). In the solid, there is only a slight difference between results calculated with and without Fermi surface blurring. In the liquid, the result calculated with $\Delta k_F/k_F = 10\%$ has greatly improved agreement with the experimental result compared to the result calculated with $\Delta k_F/k_F = 1.2\%$. The

[1] We estimated Δk_F in the Green function method [76] using the following relation: $n(k_F + \Delta k_F)/n(k_F) = [1/(e+1)] \cdot [1/(1+1)]^{-1}$, where we assumed that the momentum distribution function is expressed as $n(k) = 1/\exp\left[\frac{E(k)-E(k_F)}{\Delta}\right]$ (Δ describes the blurring of the Fermi surface [73]).

effect of Fermi surface blurring affects the derivative of $\chi(q,0)$, as seen in Fig. 4.19: the feature of the $2k_F$ singularity is broadened with increasing $\Delta k_F/k_F$. This trend is qualitatively consistent with that for the experimentally obtained $\Delta\chi(q,0)/\Delta q$. Thus, we have experimentally demonstrated that Fermi surface blurring is essential for describing screening in the disordered liquid state.

We comment on the effect of the core electrons on $\chi(q,0)$. In fact, $\chi(q,0)$ is influenced by the contribution of the core electrons excitation through the K–K relation. Figs. 4.20(a) and (b) show the integrand of the K–K relation ($\mathrm{Im}[\chi(q,\omega)]/\omega$). The contribution of the core electrons excitation, in $\hbar\omega > 55$ eV, grows with increasing q, and this contribution is not negligible in $q > 2k_F$.

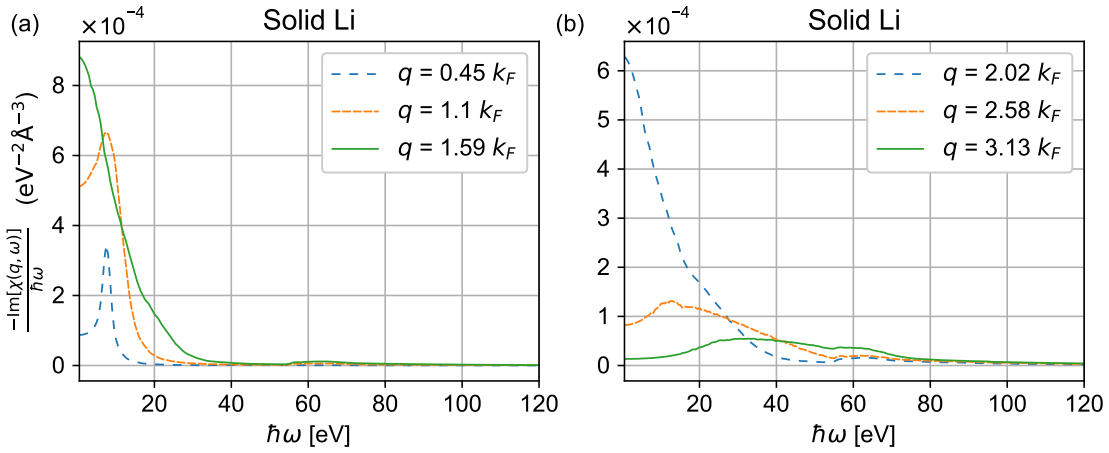

Figure 4.20: (a) $\frac{-\mathrm{Im}[\chi(q,\omega)]}{\hbar\omega}$ of solid Li in low q region and (b) high q region.

In principle, information on the many-body effects, which is described with $G(q)$, can be deduced from experimentally determined $\chi(q,0)$. The density response function $\chi(q,0)$ is constructed from $\chi_0(q,0)$ and $G(q)$ (See Eq. (4.3)). $\chi_0(q,0)$ depends on the single-particle state of Li, which can be calculated with DFT calculation [77,78]. Theoretical calculation of $\chi_0(q,0)$ for Li provides an opportunity for the direct ex-

perimental examination of $G(q)$ using Eq. (4.3). We hope this work will stimulate further theoretical work.

4.3.4 Screening Electron Density

To investigate screening in real space, we have calculated the screening electron density $\Delta n(r)$ using $\chi(q,0)$ [64]:

$$\Delta n(r) = \frac{1}{2\pi^2}\int_0^\infty dq \left(\frac{q\sin qr}{r}\right)\chi(q,0)\frac{4\pi e(-e)}{q^2}, \tag{4.8}$$

where we assumed the external potential of a positive point charge. As the q range of the experimental results is limited, we extrapolated the data using the response function of the electron gas model within the RPA. Figure 4.21 shows the extrapolated results. The extrapolated curve well reproduces the q dependence of the experimental results.

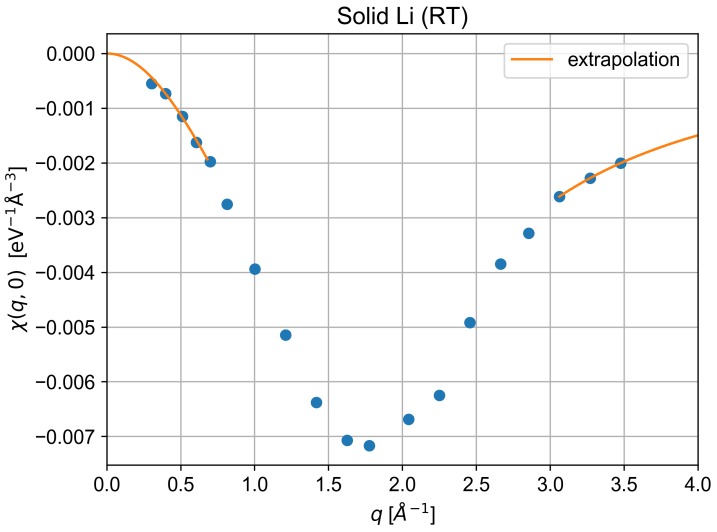

Figure 4.21: Extrapolation of $\chi(q,0)$ for solid Li.

Figure 4.22 shows the calculated screening electron density. The electrons ag-

gregate to the positive charge at $r = 0$, and they form the screening cloud in the range of about 2.2 Å, which is estimated from the distance at which $\Delta n(r)$ decays to 1 % of $\Delta n(0)$. Figure 4.23(a) shows an enlargement of $\Delta n(r)$. In addition to the screening near at $r = 0$, electron density oscillations over a long range have been observed. To examine the relation between the oscillations and the $2k_F$ singularity, we estimated the wave vector of the oscillations from the distance between the maximum and minimum positions, and obtained $K_{\mathrm{Sol}} = (2.20 \pm 0.35)k_F$ and $K_{\mathrm{Liq}} = (2.39 \pm 0.63)k_F$. We also estimated the wave vector from the peaks in $r > 5$ Å, because the Friedel oscillations are regarded as density oscillations at large r. The estimation in $r > 5$ Å shows $K_{\mathrm{Sol}} = (2.04 \pm 0.19)k_F$ and $K_{\mathrm{Liq}} = (1.99 \pm 0.27)k_F$, and these reasonably agree with the wave vector of the Friedel oscillations.

It is noted that in the liquid the Friedel oscillations are smaller than in the solid. This difference should be related to the sharpness of the Fermi surface. We calculated $\Delta n(r)$ which includes the effect of Fermi surface blurring, and Figure 4.23(b) shows the calculated results of $\Delta n(r)$. The damping of the Friedel oscillations is enhanced with increasing $\Delta k_F/k_F$, and the amplitude of the Friedel oscillations with $\Delta k_F/k_F = 10\%$ is particularly small. This qualitatively reproduces the experimental trend of $\Delta n(r)$ upon melting. Thus, the Friedel oscillations in the liquid state are weaker than in the solid because of the Fermi surface blurring.

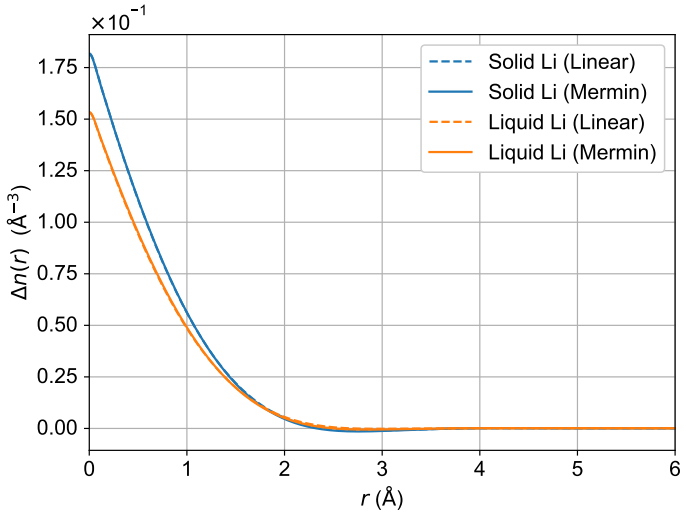

Figure 4.22: Screening electron density of Li near the positive point charge.

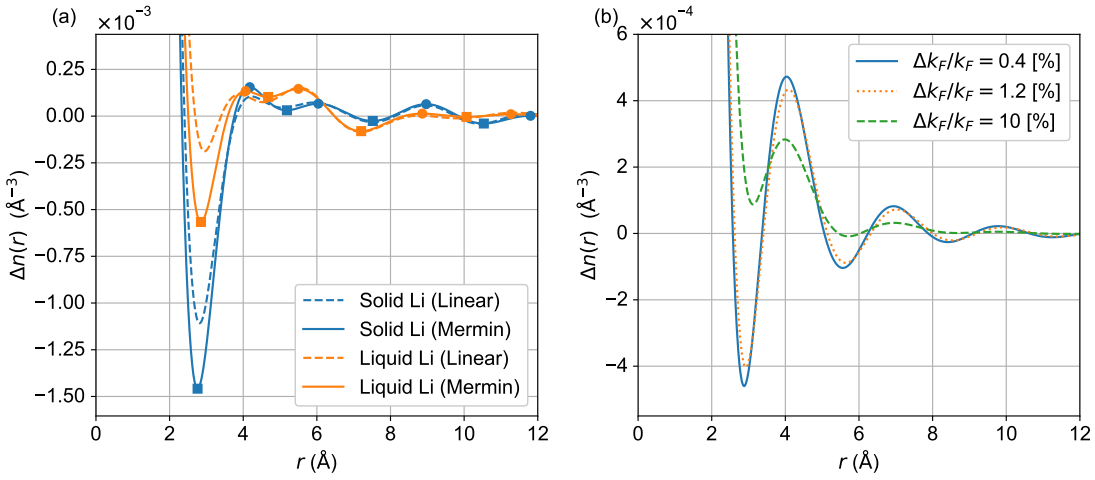

Figure 4.23: (a) Enlargement of the long-range oscillations in $\Delta n(r)$. For $\Delta n(r)$ calculated by the BM extrapolation method, the maximum and minimum positions of oscillations are indicated by circles and squares, respectively. (b) Calculated $\Delta n(r)$ including the effect of Fermi surface blurring.

4.3.5 Static Dielectric Function

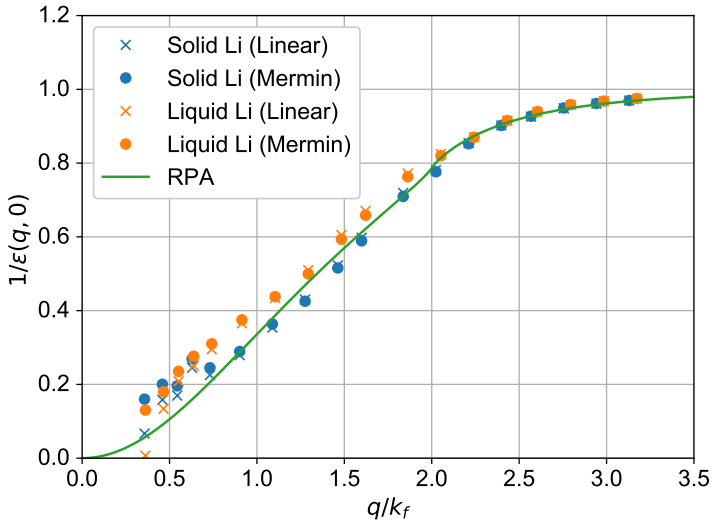

Figure 4.24: Inverse of the static dielectric function of solid Li. The solid line represents that of the electron gas model within the RPA (Lindhard dielectric function).

Finally, we derive the static dielectric function based on Eq. (1.5). The dielectric function may be more familiar than the density response function, because it is explained in standard text books of solid state physics [69, 79, 80]. Figure 4.24 shows $1/\varepsilon(q,0)$ of solid and liquid Li. In $q < 0.5k_F$, the errors seem to be large compared to the data at high q, because of q^{-2} factor in Eq. (1.5). $1/\varepsilon(q,0)$ of the solid and liquid increases with q and approach to 1 in high q region, which means that the screening effect becomes weak as the q increases. We have compared the experimentally obtained $1/\varepsilon(q,0)$ with the static Lindhard dielectric function. For nearly half a century, the static Lindhard dielectric function has been used in the field of condensed matter physics, but this is the first comparison of the static Lindhard dielectric function with the experimentally obtained results. The q dependence of the experimentally obtained $1/\varepsilon(q,0)$ shows a reasonable agreement

with the Lindhard results, as in the case of $\chi(q,0)$. Although further calculation including the effect of the core electrons is desired, we experimentally demonstrate that a basic property of screening in a simple metal is well described by the static Lindhard dielectric function.

4.4 Summary

We performed IXS experiments on solid and liquid Li to determine the static density response function. The experimentally determined $\chi(q,0)$ exhibits the $2k_F$ singularity predicted in the electron gas model. Using $\chi(q,0)$, we calculated the screening electron density and found that the amplitude of the Friedel oscillations in the liquid is smaller than in the solid. This trend upon melting is explained by Fermi surface blurring arising from the disordered scattering effect.

The experimentally obtained $\chi(q,0)$ of a simple metal provides a testing ground for the theoretical description of screening, and will provide valuable insight into the many-body effects in the density functional theory. Moreover, the static density response function is connected with effective interionic potential, which plays a central role in molecular dynamics simulation, and the density response function will be useful to construct the effective interionic potential in metals.

Chapter 5

Conclusion

In this thesis, we have carried out IXS experiments on liquid alkali metals to form the foundation of a experimental approach for studying the electronic excitation and static dielectric screening of liquid metals, which are described by $\varepsilon(q, \omega)$ or $\chi(q, \omega)$.

In Chapter 3, the IXS spectra of liquid Rb at high temperatures are presented, and we determined the density dependence of the plasmon energy and line width from the spectra. We found that the density dependence of the plasmon energy is well described by the electron gas model, however, the absolute value is lower than that of the electron gas model. We have calculated the plasmon energy of liquid Rb at $q = 0$ including the effect of ionic structure, and showed that the effect of ionic structure is important for reproducing the experimental results. We compared the experimentally obtained plasmon line width with that of the electron gas model. The agreement between the calculated and the experimental results is greatly improved if the effect of ionic structure is included. The obtained information on the plasmon in the high temperature region is valuable for understanding the relationship between the ionic structure and the electronic state.

In Chapter 4, we measured IXS spectra of solid and liquid Li to determine the static density response function. The experimentally obtained $\chi(q, 0)$ exhibits the

$2k_F$ singularity, which reflects the sharp cutoff in the momentum distribution of Li. Using $\chi(q,0)$, we calculated the screening electron density induced by a positive point charge, the calculated screening electron density shows the Friedel oscillations both in the solid and liquid. The amplitude of the Friedel oscillation becomes small upon melting. With the aid of theoretical calculations, we showed that this trend is attributed to Fermi surface blurring due to the disordered scattering effect. The experimentally determined density response function provides a testing ground for the theoretical description of dielectric screening, and will contribute the refinement of the many-body effects in the density functional theory.

In this thesis, we have laid the foundation of for experimentally investigating the electronic excitation and static dielectric screening of liquid metals. We found that the plasmon energy reflects the information on the electron density and liquid structure. Thus, the observation of the plasmon in lower density state provides valuable insight into the physics underlying the charge inhomogeneity in fluid alkali metals. Moreover, the experimental determination of $\varepsilon(q,0)$ and $\chi(q,0)$ in the low-density fluid alkali metals will offer an opportunity to clarify the problem of the instability of the low-density electron gas.

Appendix A

A.1 Density Response Function

The density response function $\chi(\boldsymbol{r}, \boldsymbol{r}', t)$ is defined as [11]

$$\chi(\boldsymbol{r}, \boldsymbol{r}', t) = -\frac{i}{\hbar}\theta(t)\langle[\hat{n}(\boldsymbol{r}, t), \hat{n}(\boldsymbol{r}', 0)]\rangle, \tag{5.1}$$

where $\hat{n}(\boldsymbol{r}, t)$ is the number density operator and $\theta(t)$ is the step function equal to 1 for $t > 0$, and 0 otherwise. $\langle \cdots \rangle$ denotes the average in the thermal equilibrium ensemble:

$$\langle \hat{A} \rangle = \frac{1}{Z} \sum_n e^{-\beta E_n} \langle \psi_n | \hat{A} | \psi_n \rangle, \tag{5.2}$$

where Z is the canonical partition function, and $|\psi_n\rangle$ is the eigenstate of the unpurterbed Hamiltonian. $\chi(\boldsymbol{r}, \boldsymbol{r}', t)$ describes the electron density induced by external potential $V_{\text{ext}}(\boldsymbol{r}, t)$:

$$\Delta n(\boldsymbol{r}, t) = \int_{-\infty}^{\infty} d\tau \int d\boldsymbol{r}' \chi(\boldsymbol{r}, \boldsymbol{r}', \tau) V_{\text{ext}}(\boldsymbol{r}', t - \tau). \tag{5.3}$$

The step function in Eq. (5.1) guarantees the causality, and the induced electron density at time t arises from $V_{\text{ext}}(\boldsymbol{r}', t')$ for $t' < t$. The definition of the density response function in the $\boldsymbol{r}$ and t representation is easy to understand intuitively, however, an actual calculation of the density response function is usually carried

out in $\boldsymbol{q}$ and ω space. The space and time Fourier transform of $\chi(\boldsymbol{r}, \boldsymbol{r}', t)$ is given by

$$\chi(\boldsymbol{q}, \boldsymbol{q}', \omega) = \frac{1}{V} \int d\boldsymbol{r} \int d\boldsymbol{r}' \int_{-\infty}^{\infty} dt \chi(\boldsymbol{r}, \boldsymbol{r}', t) e^{i(\boldsymbol{q}' \cdot \boldsymbol{r}' - \boldsymbol{q} \cdot \boldsymbol{r})} e^{i\omega t}, \tag{5.4}$$

and the relation with the induced density is expressed as

$$\Delta n(\boldsymbol{q}, \omega) = \chi(\boldsymbol{q}, \boldsymbol{q}', \omega) V_{\text{ext}}(\boldsymbol{q}', \omega). \tag{5.5}$$

In translationally invariant systems, only the $\boldsymbol{q} = \boldsymbol{q}'$ component of $\chi(\boldsymbol{q}, \boldsymbol{q}', \omega)$ is nonzero, and Eq. (5.5) is simplified:

$$\Delta n(\boldsymbol{q}, \omega) = \chi(\boldsymbol{q}, \omega) V_{\text{ext}}(\boldsymbol{q}, \omega), \tag{5.6}$$

where we define $\chi(\boldsymbol{q}, \omega) \equiv \chi(\boldsymbol{q}, \boldsymbol{q}, \omega)$.

Appendix B

B.1 Lindhard Dielectric Function

The Lindhard dielectric function is expressed as

$$\varepsilon(q,\omega) = 1 + \frac{8\pi e^2}{q^2} \sum_{\boldsymbol{k}} \frac{f(\boldsymbol{k}) - f(\boldsymbol{k}+\boldsymbol{q})}{E(\boldsymbol{k}+\boldsymbol{q}) - E(\boldsymbol{k}) - \hbar\omega - i\eta}, \tag{5.7}$$

where $E(\boldsymbol{k}) = \hbar^2 k^2/(2m)$ is the energy of the free electrons and $f(\boldsymbol{k})$ is the Fermi-Dirac distribution function. The summation in Eq. (5.7) can be analytically evaluated. The real and imaginary part are written as [69]

$$\begin{aligned}
\mathrm{Re}[\varepsilon_{\mathrm{L}}(q,\omega)] \quad &= 1 + \frac{2me^2}{\pi\hbar^2}\frac{k_F}{q^2} + \frac{me^2}{\pi\hbar^2}\frac{1}{q^3}\left[k_F^2 - \left(\frac{q}{2} - \frac{m\omega}{\hbar q}\right)^2\right] \\
&\quad \times \ln\left|\frac{2qk_F + q^2 - 2m/\hbar)\omega}{-2qk_F + q^2 - 2m/\hbar)\omega}\right| \\
&\quad + \frac{me^2}{\pi\hbar^2}\frac{1}{q^3}\left[k_F^2 - \left(\frac{q}{2} + \frac{m\omega}{\hbar q}\right)^2\right] \ln\left|\frac{2qk_F + q^2 + 2m/\hbar)\omega}{-2qk_F + q^2 + 2m/\hbar)\omega}\right|,
\end{aligned}$$

$$\mathrm{Im}\varepsilon_{\mathrm{L}}(q,\omega) = \begin{cases} \dfrac{2m^2e^2}{\hbar^3}\dfrac{\omega}{q^3} & (q < 2k_F, 0 \le \dfrac{2m}{\omega} \le 2qk_F - q^2) \\ \dfrac{me^2}{\hbar^2}\dfrac{1}{q^3}\left[k_F^2 - \left(\dfrac{q}{2} - \dfrac{m\omega}{\hbar}\dfrac{}{q}\right)^2\right] & (2qk_F - q^2 \le \dfrac{2m}{\omega} \le 2qk_F + q^2) \\ 0 & (\text{otherwise}). \end{cases}$$

In $q < q_{\mathrm{c}}$, the Lindhard function satisfies the condition $\mathrm{Re}[\varepsilon_{\mathrm{L}}(q,\omega_{\mathrm{p}}(q))] = 0$ and $\mathrm{Im}[\varepsilon_{\mathrm{L}}(q,\omega_{\mathrm{p}}(q))] = 0$. Thus, the plasmon in the electron gas is not damped within the RPA.

B.2 Mermin Dielectric Function

The Mermin dielectric function is based on the electron gas model within the RPA like the Lindhard dielectric function. In the Mermin dielectric function, the effect of the damping is included by phenomenological constant η, and the dielectric function is expressed as [75]

$$\varepsilon_{\mathrm{BM}}(q,\omega) = 1 + \frac{(1+i\eta/\omega)[\varepsilon_{\mathrm{L}}(q,\tilde{\omega}) - 1]}{1 + (i\eta/\omega)[\varepsilon_{\mathrm{L}}(q,\tilde{\omega}) - 1][\varepsilon_{\mathrm{L}}(q,0) - 1]^{-1}}, \tag{5.8}$$

where $\tilde{\omega} = \omega + i\eta$.

B.3 Static Dielectric Function with Fermi Surface Blurring

We present the static dielectric function including the effect of Fermi surface blurring proposed by Leavens *et al.* [74]. Δk_F is related to the mean free pass l, and the

dielectric function $\varepsilon(q,l)$ is written as [74]:

$$\varepsilon(q,l) = 1 + \frac{2k_F}{\pi a_B q^2} \times \left[1 - \frac{1}{2k_F l}\left\{\tan^{-1}\left(\frac{4k_F l}{1+(ql)^2-(2k_F l)^2}\right) + \pi\theta(4k_F^2 - q^2 - l^{-2})\right\} + \frac{1-(q/2k_F)^2+(2k_F l)^{-2}}{4(q/2k_F)} \ln\left\{\frac{((ql)^2+1+2k_F q l^2)^2+(2k_F l)^2}{((ql)^2+1-2k_F q l^2)^2+(2k_F l)^2}\right\}\right]. \quad (5.9)$$

where $\theta(x)$ is the step function. In the collisionless limit ($l \to \infty$), $\varepsilon(q,l)$ is equivalent to $\varepsilon_{\mathrm{L}}(q,0)$. Figure 5.1) shows the calculated results of $\varepsilon(q,l)$ for solid and liquid Li. The change of slope at $2k_F$ becomes small with increasing $\Delta k_F/k_F$.

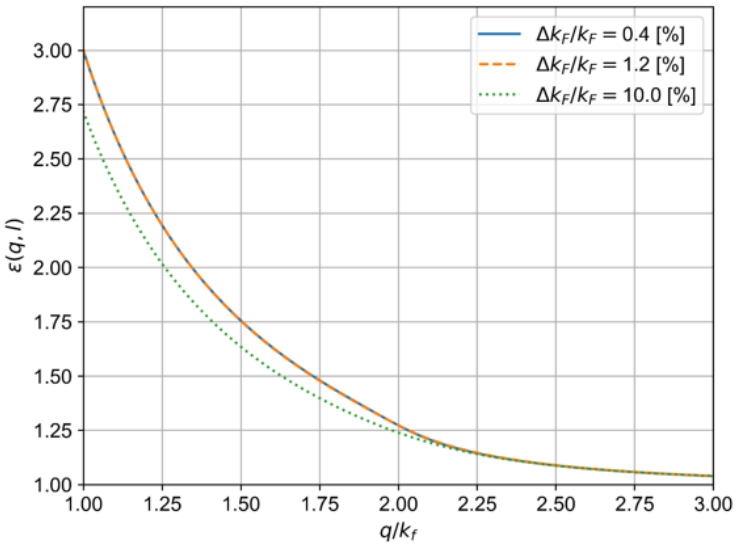

Figure 5.1: Dielectric function of Leavens *et al.* calculated for solid and liquid Li.

Acknowledgement

My deepest appreciation goes to Prof. Kazuhiro Matsuda. He taught me how to perform experimental study in the field of liquid metals as my supervisor. Moreover, he gave me sincere strong support and encouragement in the process of this study.

I would like to express my gratitude to Dr. Nozomu Hiraoka. He adjusted the optical components in the beamline BLXU at SPring-8. He gave me valuable advice on IXS techniques. Without his advice, the contents of Chapter 4 could not be completed.

I am deeply grateful to the late Makoto Yao and Professor Kiyonobu Nagaya. They provide me profound insight and comments for the experimental results. I would like to thank Prof. Masanori Inui and Prof. Yukio Kajihara, who helped IXS experiments at SPring-8. In addition, discussions with them have been insightful.

I would particularly like to thank Prof. Koji Kimura, who taught me carefully about experimental techniques and how to analyze IXS data in the laboratory. I want to thank the students of the laboratory, Mr. T. Nishiyama, Y. Ishiguro, T. Miyatake, H. Hayashi, M. Watanabe, A. Niozu, N. Yokono, T. Sakurazawa, Y. Jeong, and A. Yamamoto, with whom I carried out experiments and discussion. Their experimental supports and discussion were invaluable.

This work was supported by JSPS KAKENHI (Research Nos. 24540401, 15K05209, and 18H01142) and the Toray Science Foundation. The synchrotron radiation experiments were performed at SPring-8 with the approval of the National Synchrotron

Radiation Research Center, Taiwan (Proposal Nos. 2015-2-100-1, 2015-3-061-1, 2015-3-061-3, 2015-3-061-4, 2017-2-215-1, 2017-3-250-1, 2018-1-229-1, 2018-2-189-1, and 2018-3-180-1) and Japan Synchrotron Radiation Research Institute (Proposal Nos. 2015A4264, 2015B4251, 2016A4264, 2016B4254, 2017A4267, 2017B4254, 2018A4253, 2018A4261, and 2018B4260).

Finally, I would like to thank my family for long-term support.

Bibliography

[1] T. C. Chi: J. Phys. Chem. Ref. Data **8** (1979) 339.

[2] J. M. Ziman: Phil. Mag. **6** (1961) 1013.

[3] F. Noll, W.-C. Pilgrim, and R. Winter: Z. Phys. Chem. N F **156** (1998) 303.

[4] W. Freyland: J. Phys. Colloq. **74** (1980) C8.

[5] B. Knuth, F. Hensel, and W. W. Warren: J. Phys.: Condens. Matter **9** (1997) 2693.

[6] K. Matsuda, K. Tamura, and M. Inui: Phys. Rev. Lett. **98** (2007) 096401.

[7] F. Shimojo and Y. Zempo: Phys. Rev. B **52** (1995) 9320.

[8] K. Matsuda, K. Kimura, T. Nagao, T. Hagiya, Y. Kajihara, M. Inui, K. Tamura, M. Katoh, M. Itou, N. Hiraoka, and Y. Sakurai: EPL (Europhysics Letters) **117** (2017) 17004.

[9] W.-C. Pilgrim, D. Szubrin, F. Demmel, A. Orecchini, S. Rols, A. Laloni, and A. D. Francesco: EPL (Europhysics Letters) **122** (2018) 36005.

[10] D. M. Ceperley and B. J. Alder: Phys. rev. B **45** (1980) 566.

[11] G. Giuliani and G. Vignale: *Quantum Theory of the Electron Liquid* (Cambridge University Press, 2005).

[12] L. V. Keldysh, D. A. Kirzhnitz, and A. A. Maradudin: *The Dielectric Function of Condensed Systems* (North-Holland, Amsterdam, 1989), p. 64.

[13] S. Ichimaru: Rev. Mod. Phys. **54** (1982) 1017.

[14] K. Utsumi and S. Ichimaru: Phys. Rev. B **24** (1981) 3220.

[15] P. Vashishta and K. S. Singwi: Phys. Rev. B **6** (1972) 875.

[16] W. Schülke: *Electron Dynamics by Inelastic X-ray Scattering* (Oxford University Press, 2007).

[17] P. Neumayer, C. Fortmann, T. Döppner, P. Davis, R. W. Falcone, A. L. Kritcher, O. L. Landen, H. J. Lee, R. W. Lee, C. Niemann, S. Le Pape, and S. H. Glenzer: Phys. Rev. Lett. **105** (2010) 075003.

[18] P. Sperling, E. J. Gamboa, H. J. Lee, H. K. Chung, E. Galtier, Y. Omarbakiyeva, H. Reinholz, G. Röpke, U. Zastrau, J. Hastings, L. B. Fletcher, and S. H. Glenzer: Phys. Rev. Lett. **115** (2015) 115001.

[19] I. Loa, K. Syassen, G. Monaco, G. Vankó, M. Krisch, and M. Hanfland: Phys. Rev. Lett. **107** (2011) 086402.

[20] H.-K. Mao, Y. Ding, Y. Xiao, P. Chow, J. Shu, S. Lebegue, A. Lazicki, and R. Ahuja: Proc. Natl. Acad. Sci. U.S.A. **108** (2011) 20434.

[21] P. Abbamonte, K. D. Finkelstein, M. D. Collins, and S. M. Gruner: Phys. Rev. Lett. **92** (2004) 237401.

[22] P. Abbamonte, G. Wong, D. Cahill, J. Reed, R. Coridan, N. Schmidt, G. Lai, Y. Joe, and D. Casa: Adv. Mater. **22** (2010) 1141.

[23] K. Sturm: Z. Naturforsch. **48a** (1993) 233.

[24] P. Abbamonte, T. Graber, J. P. Reed, S. Smadici, C.-L. Yeh, A. Shukla, J.-P. Rueff, , and W. Ku: PNAS **105** (2008) 12159.

[25] J. P. Reed, B. Uchoa, Y. I. Joe, Y. Gan, D. Casa, E. Fradkin, and P. Abbamonte: Science **330** (2010) 805.

[26] K. Tamura, M. Inui, and S. Hosokawa: Rev. Sci. Instrum. **70** (1999) 144.

[27] K. Kimura: Ph.D. thesis, Kyoto University (2015).

[28] Y. Q. Cai, P. Chow, C. C. Chen, H. Ishii, K. L. Tsang, C. C. Kao, K. S. Liang, and C. T. Chen: AIP Conf. Proc. **705** (2004) 340.

[29] N. Hiraoka, H. Fukui, H. Tanida, H. Toyokawa, Y. Q. Cai, and K. D. Tsuei: J. Synchrotron Rad. **20** (2013) 266.

[30] P. Eisenberger, P. M. Platzman, and P. Schmidt: Phys. Rev. Lett. **34** (1975) 18.

[31] G. D. Priftis, J. Boviatsis, and A. Vradis: Phys. Lett. A **68** (1978) 482.

[32] H. Nagasawa, S. Mourikis, and W. Schülke: J. Phys. Soc. Jpn **58** (1989) 710.

[33] W. Schülke, H. Nagasawa, and S. Mourikis: Phys. Rev. Lett. **52** (1984) 2065.

[34] W. Schülke, H. Nagasawa, S. Mourikis, and P. Lanzki: Phys. Rev. B **33** (1986) 6744.

[35] J. P. Hill, C. C. Kao, W. A. C. Caliebe, D. Gibbs, and J. B. Hastings: Phys. Rev. Lett. **77** (1996) 3665.

[36] D. Pines: *Elementary Excitations in Solids* (Benjamin, New York, 1963).

[37] A. vom Felde, J. Sprösser-Prou, and J. Fink: Phys. Rev. **40** (1989) 10181.

[38] F. Aryasetiawan and K. Karlsson: Phys. Rev. Lett. **73** (1994) 1679.

[39] G. Tirao, G. Stutz, V. M. Silkin, E. V. Chulkov, and C. Cusatis: J. Phys.: Condens. Matter **19** (2007) 046207.

[40] S. Huotari, C. Sternemann, M. C. Troparevsky, A. G. Eguiluz, M. Volmer, H. Sternemann, H. Müller, G. Monaco, and W. Schülke: Phys. Rev. B **80** (2009) 155107.

[41] A. A. Quong and A. G. Eguiluz: Phys. Rev. Lett. **70** (1993) 3955.

[42] X. Zubizarreta, V. M. Silkin, and E. V. Chulkov: Phys. Rev. B **87** (2013) 115112.

[43] C. Sternemann, A. Kaprolat, and W. Schülke: Phys. Rev. B **57** (1998) 622.

[44] K. Kimura, K. Matsuda, N. Hiraoka, T. Fukumaru, Y. Kajihara, M. Inui, , and M. Yao: Phys. Rev. B **89** (2014) 014206.

[45] K. Kimura, K. Matsuda, N. Hiraoka, Y. Kajihara, T. Miyatake, Y. Ishiguro, T. Hagiya, M. Inui, and M. Yao: J. Phys. Soc. Jpn. **84** (2015) 084701.

[46] K. Kimura, K. Matsuda, and M. Yao: J. Phys. Soc. Jpn. **82** (2013) 115001.

[47] J. Lindhard: K. Dan. Vidensk. Selsk. Mat. Fys. Medd. **28** (1954) 3.

[48] S. Moroni, D. M. Ceperley, and G. Senatore: Phys. Rev. Lett. **75** (1995) 689.

[49] M. Corradini, R. D. Sole, G. Onida, , and M. Palummo: Phys. Rev. B **57** (1998) 14569.

[50] S. Chattopadhyay, B. K. Mani, , and D. Angom: Phys. Rev. A **87** (2013) 042520.

[51] K. Sturm: Adv. Phys. **31** (1982) 1.

[52] G. D. Mahan: *Many-Particle Physics* (Kluwer Academic/Plenum, New York, 2000).

[53] F. A. Oliveira and A. Ferraz: Solid State Commun. **52** (1984) 963.

[54] G. Franz, W. Freyland, W. Glaser, F. Hensel, and E. Schneider: J. Phys. Colloq. **8** (1970) 194.

[55] R. W. Ohse: *Handbook of Thermodynamic and Transport Properties of Alkali Metals* (Blackwell, Oxford, 1980), p. 316.

[56] N. W. Ashcroft: Phys. Lett. **23** (1966) 48.

[57] W. A. Harrison: *Electronic Structure and the Properties of Solids* (Freeman, San Francisco, 1980), p. 362.

[58] G. F. Giuliani and G. E. Simion: Solid State Commun. **127** (2003) 789.

[59] N. E. Cusack: *The physics of structurally disordered matter* (Adam Hilger, Bristol, 1987), p. 163.

[60] Z. Qian and G. Vignale: Phys. Rev. B **65** (2002) 235121.

[61] J. Friedel: Nuovo Cimento Suppl. **7** (1958) 287.

[62] M. F. Crommie, C. P. Lutz, and D. M. Elgler: Nature (London) **363** (1993) 524.

[63] Y. Hasegawa and P. Avouris: Phys. Rev. Lett. **71** (1993) 1071.

[64] G. E. Simion and G. F. Giuliani: Phys. Rev. B **72** (2005) 045127.

[65] M. D. Johnson and N. H. March: Phys. Lett. **3** (1963) 313.

[66] J.-P. Hansen and I. R. McDonald: *Theory of Simple Liquids, 3rd ed.* (Academic, 2005).

[67] K. Hoshino, F. Shimojo, and M. Watabe: J. Phys. Soc. Jpn. **63** (1994) 2185.

[68] N. E. Cusack: *The Physics of Structurally Disordered Matter* (Hilger, 1987).

[69] G. Grosso and G. P. Parravicini: *Solid State Physics, 2nd ed.* (Academic, 2014).

[70] S. Huotari, M. Cazzaniga, H.-C. Weissker, T. Pylkkänen, H. Müller, L. Reining, G. Onida, and G. Monaco: Phys. Rev. B **84** (2011) 075108.

[71] D. R. Gustafson, A. R. Mackintosh, and D. J. Zaffarano: Phys. Rev. **130** (1963) 1455.

[72] A. T. Stewart, J. H. Kusmiss, and R. H. March: Phys. Rev. **132** (1963) 495.

[73] T. Gaskell and N. H. March: Phys. Lett. **7** (1963) 169.

[74] C. R. Leavens, A. H. Macdonald, R. Taylor, A. Ferraz, and N. H. March: Phys. Chem. Liq. **11** (1981) 115.

[75] N. D. Mermin: Phys. Rev. B **1** (1970) 2362.

[76] X. Z. Yan: Phys. Rev. B **51** (1995) 15823.

[77] F. Aryasetiawan and O. Gunnarsson: Phys. Rev. B **49** (1994) 16214.

[78] A. Fleszar, R. Stumpf, and A. G. Eguiluz: Phys. Rev. B **55** (1997) 2068.

[79] N. W. Ashcroft and N. D. Mermin: *Solid State Physics* (Thomson Learning, 1976), p. 8.

[80] J. M. Ziman: *Principles of the Theory of Solids, 2nd ed.* (Cambridge University Press, 1972).